



HAL
open science

In situ space plasma diagnostics with finite amplitude active electric experiments: Non-linear plasma effects and instrumental performance of mutual impedance experiments

Luca Bucciantini, P. Henri, G. Wattieaux, F. Califano, Xavier Vallières, O. Randriamboarison

► To cite this version:

Luca Bucciantini, P. Henri, G. Wattieaux, F. Califano, Xavier Vallières, et al.. In situ space plasma diagnostics with finite amplitude active electric experiments: Non-linear plasma effects and instrumental performance of mutual impedance experiments. *Journal of Geophysical Research Space Physics*, 2022, 127 (12), pp.e2022JA030813. 10.1029/2022JA030813 . insu-03882466

HAL Id: insu-03882466

<https://insu.hal.science/insu-03882466>

Submitted on 2 Dec 2022

HAL is a multi-disciplinary open access archive for the deposit and dissemination of scientific research documents, whether they are published or not. The documents may come from teaching and research institutions in France or abroad, or from public or private research centers.

L'archive ouverte pluridisciplinaire **HAL**, est destinée au dépôt et à la diffusion de documents scientifiques de niveau recherche, publiés ou non, émanant des établissements d'enseignement et de recherche français ou étrangers, des laboratoires publics ou privés.

In situ space plasma diagnostics with finite amplitude active electric experiments: non-linear plasma effects and instrumental performance of mutual impedance experiments

L. Bucciardini¹, P. Henri^{1,2}, G. Wattieaux³, F. Califano⁴, X. Vallières¹, O. Randriamboarison¹

¹Laboratoire de Physique et Chimie de l'Environnement et de l'Espace (LPC2E), CNRS, Université d'Orléans, Orléans, France

²Laboratoire Lagrange, OCA, UCA, CNRS, Nice, France

³Laboratoire Plasma et Conversion d'Énergie (LAPLACE), CNRS, Université de Toulouse, Toulouse, France

⁴Dipartimento di Fisica, Università di Pisa, Pisa, Italy

Key Points:

- The plasma response to large antenna emission amplitudes triggering non-linear plasma perturbations is simulated
- Ion dynamics contributions to large amplitude propagating electric signals in the plasma are crucial and therefore should not be neglected
- Mutual impedance diagnostic performances are acceptable for emission amplitudes corresponding to electric-to-kinetic energy ratios up to 0.1

Corresponding author: Luca Bucciardini, luca.bucciardini@cnrs.fr

This article has been accepted for publication and undergone full peer review but has not been through the copyediting, typesetting, pagination and proofreading process, which may lead to differences between this version and the [Version of Record](#). Please cite this article as [doi: 10.1029/2022JA030813](https://doi.org/10.1029/2022JA030813).

This article is protected by copyright. All rights reserved.

Abstract

Mutual impedance experiments are a kind of plasma diagnostic techniques for the identification of the in situ plasma density and electron temperature. These plasma parameters are retrieved from mutual impedance spectra, obtained by perturbing the plasma using a set of electric emitting antennas and, simultaneously, retrieving using a set of electric receiving antennas the electric fluctuations generated in the plasma.

Typical mutual impedance experiments suppose a linear plasma response to the electric excitation of the instrument. In the case of practical space applications, this assumption is often broken: low temperature plasmas, which are usually encountered in ionized planetary environments (e.g. RPC-MIP instrument onboard the Rosetta mission, RPWI/MIME experiment onboard the JUICE mission), force towards significant perturbations of the plasma dielectric.

In this context, we investigate mutual impedance experiments relaxing, for the first time, the assumption of linear plasma perturbations: we quantify the impact of large antenna emission amplitudes on the (i) plasma density and (ii) electron temperature diagnostic performance of mutual impedance instruments.

We use electrostatic 1D-1V full kinetic Vlasov-Poisson numerical simulations. First, we simulate the electric oscillations generated in the plasma by mutual impedance experiments. Second, we use typical mutual impedance data analysis techniques to compute the mutual impedance diagnostic performance in function of the emission amplitude and of the emitting-receiving antennas distance.

We find the plasma density and electron temperature identification processes robust (i.e. relative errors below 5% and 20%, respectively) to large amplitude emissions for antenna emission amplitudes corresponding to electric-to-thermal energy ratios up to $(\epsilon_0 E^2) / (n_0 k_B T_e) = 0.1$.

1 Introduction

Mutual impedance (hereafter MI) experiments are a kind of in situ plasma diagnostic instruments that enable measurements of the absolute plasma density and the electron temperature through the dynamical response of a probed plasma to an external electrical excitation. Such measurement techniques were proven successful for several ionospheric (Storey et al., 1969; Béghin & Debie, 1972; Pottelette et al., 1975; Décréau et al., 1978; Pottelette & Storey, 1981; Bahnsen et al., 1988; Grard, 1997) (e.g. ISOPROBE experiment onboard the AUREOL-3 satellite, for the ARCAD-3 mission Béghin et al., 1982) and planetary space missions (e.g. the RPC-MIP instrument, J. Trotignon et al., 2007, on board the ESA Rosetta mission). Different versions of MI experiments will also contribute to new exploratory missions such as the joint ESA-JAXA BepiColombo mission with the PWI/AM2P experiment (Kasaba et al., 2020; J. Trotignon et al., 2006), the JUICE ESA mission with the RPWI/MIME experiment and the Comet Interceptor ESA mission with the DFP-COMPLIMENT instrument (Snodgrass & Jones, 2019). New versions of MI experiments are currently being developed to adapt to the constraints of nano/microsatellite platforms.

The basic principle of MI experiments is the following. Plasma parameters such as the electron density and temperature are obtained through the analysis of the so-called MI spectrum. It is defined as the electrical impedance between an emitting and a receiving electric antenna embedded in the plasma to be diagnosed (Storey et al., 1969; Chasseriaux et al., 1972; Béghin, 1995; Gilet et al., 2017; Wattiaux, G. et al., 2019). Practically, the electron density and temperature are derived as follows. The plasma environment is perturbed by the emission of a succession of elementary electric sinusoidal oscillations injected in the plasma through the emitting electric antennas. Simultaneously,

69 the electric oscillations that propagate in the probed plasma are measured with the re-
70 ceiving antennas. Such oscillations correspond to the plasma response at the emitted fre-
71 quency. This frequency is modified step by step to cover a given range of frequencies and
72 build up the MI spectrum. We hereafter refer to this process as frequency sweep. The
73 MI spectrum is a function of the plasma dielectric and it exhibits resonant signatures
74 at the plasma characteristic frequencies (plasma eigenmodes). For instance, in the case
75 of an unmagnetized plasma, MI spectra present one resonant signature at the plasma
76 frequency. The electron density and the temperature are retrieved from the position and
77 the shape of the resonance, respectively (Chassériaux, 1972; Chassériaux, 1974).

78 The state-of-the-art methods used to model the instrumental response of MI ex-
79 periments consider a variety of situations or processes known to significantly impact the
80 instrumental response: (i) in collisionless plasmas, various types of distribution functions
81 that account for different plasma populations (Gilet et al., 2017; Wattieaux, G. et al.,
82 2019), (ii) the peculiar boundary conditions imposed by a conductive spacecraft carry-
83 ing the experiment (Geiswiler et al., 2001) and (iii) the influence of spacecraft charg-
84 ing that generates a plasma sheath surrounding the spacecraft and the instrument (Wattieaux,
85 G. et al., 2019). These models are all based on the assumption of a linear response of
86 the plasma to the electric excitation of the instrument. This means that such models as-
87 sume that the emitting antennas introduce small enough electric perturbations within
88 the plasma, so that its dynamics is defined by its linear dielectric (Grard, 1969). There-
89 fore, they assume negligible non-linear effects triggered by the emission process. Hence,
90 they assume that the electric energy injected by the emitting antenna is much smaller
91 than the thermal energy of the plasma to be diagnosed.

92 To ensure small perturbations of the plasma dielectric, MI experiments are designed
93 to emit low amplitude signals. Practically, this is done by limiting the voltage imposed
94 on the emitting antenna. This also has the advantage of limiting the electric power con-
95 sumption required for MI space experiments.

96 However, the voltage imposed on the emitting antenna can not be too small to en-
97 sure a satisfactory signal-to-noise ratio.

98 First, the amplitude of the received signal is proportional to that of the emitted
99 signal. A large enough emitted signal therefore corresponds to an increased amplitude
100 for the received signal. Strong emissions are particularly needed if the distance between
101 emitting and receiving antenna is large. This is the case for MI instruments designed to
102 probe hot space plasmas, e.g. with particles energy of the order of 10 eV. For instance,
103 the so-called LDL mode of the RPC-MIP instrument on Rosetta designed to observe hot
104 plasmas near comet 67P/CG, the PWI/AM2P experiment on BepiColombo that will mon-
105 itor hot plasmas in Mercury's environment and the RPWI/MIME experiment on JUICE
106 that will investigate hot plasmas in the ionosphere of Ganymede.

107 Second, the instrument design must ensure that the received signal is above the in-
108 strumental noise. Instrumental noise is essentially composed of two main sources. On
109 the one hand, the background noise of the instrument itself. On the other hand, the over-
110 all electrical noise generated by the platform and the rest of the payload. This second
111 source is often referred to as the electromagnetic compatibility (EMC) of the spacecraft
112 (ECSS-E-ST-20-07C handbook of ECSS, Youssef, 1996). EMC is costly for standard plat-
113 forms and particularly delicate for nanosatellite platforms. Sufficiently large amplitude
114 emission signals therefore mitigate the lack of EMC by improving the signal-to-noise ra-
115 tio. It is therefore expected that large amplitude emissions might be preferable for fu-
116 ture MI experiments designs, especially those dedicated to nanosatellite platforms.

117 On the one hand, from a practical point of view, there is therefore a net benefit in
118 increasing the amplitude of the signal emitted in the plasma to increase the signal-to-
119 noise ratio. On the other hand, from a plasma diagnostic point of view, there are net ben-
120 efits in decreasing the amplitude of the signal emitted in the plasma. First, it ensures
121 that the plasma response is described by its linear dielectric. Second, it limits the per-

122 turbations on other instruments of the payload such as interferences due to the MI emit-
123 ted signal. All in all, a trade-off is chosen to ensure a large enough signal to be measured,
124 for a small enough signal to be emitted: between few 10s mV and 1 V in typical space
125 plasmas.

126 However, even with such trade-off, the linear plasma response hypothesis is often
127 broken in ionized planetary environments, especially in dense, low-energy plasma regions.
128 A recent example is given by the cold cometary plasma probed by Rosetta in the inner
129 coma of comet 67P/CG, with electron temperatures as low as 0.1eV independently mea-
130 sured by both the MI RPC-MIP (Wattiaux et al., 2020) and the Langmuir Probe RPC-
131 LAP (Eriksson, A. I. et al., 2017; Odelstad et al., 2020). Similar situations are also ex-
132 pected to be encountered by the RPWI/MIME experiment onboard JUICE in the iono-
133 sphere of Ganymede. In such cases, the thermal energy of the electrons can hardly be
134 considered much larger than the injected electric perturbation. Hence, non-linear plasma
135 effects (e.g. wave-wave and wave-particle interactions) are expected to strongly modify
136 the plasma response to MI emissions. The assumption of a linear plasma dielectric re-
137 sponse to the instrument perturbation becomes invalid. Consequently, it is necessary to
138 assess the plasma diagnostic performance of MI experiments in such common situations.

139 In this context, the objective of this study is to assess how strong the electric emis-
140 sions can be in active in situ plasma measurements such as MI experiments, while pre-
141 venting significant losses in instrumental performance. To this purpose, this study aims
142 at relaxing, for the first time, the assumption of linear perturbations of the local plasma
143 environment in MI instrumental modeling in order to investigate the influence of the plasma
144 non-linear effects on the MI instrumental response. Practically, we aim at quantifying
145 the impact of non-linear effects on MI diagnostics by assessing the error both in electron
146 density and temperature measurements for large emission amplitudes.

147 The investigation described in this paper is performed by means of 1D-1V full ki-
148 netic numerical simulations that model the plasma response to an external electric an-
149 tenna, by solving the Vlasov-Poisson coupled equations for both ions and electrons.

150 This document is organized as follows. The numerical models adopted in this in-
151 vestigation are described in section 2. The initialization of the numerical model and its
152 validation are described in Appendix A and Appendix B, respectively. For repeatabil-
153 ity purposes, the parameters defining the numerical simulations described in this study
154 are listed in Appendix C. The non-linear effects generated in the plasma by strong elec-
155 trical antenna excitations are described in section 3, and their consequence on plasma
156 diagnostics performed by MI experiments is quantified in section 4. We conclude by dis-
157 cussing the implication for both past and current space mission data analysis, as well
158 as for future instrumental designs in section 5.

159 2 Model description: 1D-1V Vlasov-Poisson

160 We consider a non magnetized, homogeneous, collisionless plasma composed of elec-
161 trons and ions initially described by a single Maxwellian velocity distribution function.
162 An electrical antenna is used to inject an external electric field perturbation to which
163 the plasma reacts self-consistently. We neglect in our model the perturbations arising
164 from the presence of the plasma sheath surrounding the antennas used for MI measure-
165 ments.

166 The simulation models used in this study are based on the numerical integration
167 of the Vlasov-Poisson system of equations that describe the spatio-temporal evolution
168 of electron and ion distribution functions ($f_e(t, x, v_e)$ and $f_p(t, x, v_i)$), respectively, where
169 t is the time, x the position in the plasma and v the electrons and ions velocity). The
170 numerical integration scheme is the one described by Mangeney et al. (2002). The Vlasov
171 equation used to evolve in time the electron and ion distribution function, simplified con-

172 sidering a negligible magnetic field, reads:

$$173 \quad \frac{\partial f_\gamma(x, t, v_\gamma)}{\partial t} + \vec{v}_\gamma \cdot \nabla f_\gamma(x, t, v_\gamma) + \frac{q_\gamma}{m_\gamma} \vec{E} \cdot \nabla_{\vec{v}_\gamma} f_\gamma(x, t, v_\gamma) = 0 \quad (1)$$

174 where $\gamma = e, i$ represents the species and E is the electric field.

175 We limit our study to the 1D-1V electrostatic case. We use the model previously
176 used in Henri et al. (2010), modified adding multiple external emitting electric anten-
177 nas modeled using oscillating charge densities in the Poisson equation:

$$178 \quad \nabla \cdot \vec{E} = e \frac{n_i(x, t) - n_e(x, t)}{\epsilon_0} + \frac{\rho_{ext.}(x, t)}{\epsilon_0} \quad (2)$$

179 where n_e (resp. n_i) is the electron (resp. ion) density and $\rho_{ext.}$ the external charge den-
180 sity.

181 The equations are normalized using electron characteristic quantities: the elemen-
182 tary charge e , the electron mass m_e , the Debye length λ_D , the time ω_p^{-1} , with $\omega_p = \sqrt{(e^2 n_0)/(\epsilon_0 m_e)}$
183 the angular plasma frequency, and the mean density n_0 . It follows that velocities are nor-
184 malized by the electron thermal speed $v_{the} = \lambda_D \omega_p$, the electric field by $E = (m_e v_{the} \omega_p) / e$
185 and the charge density at the antenna by $\bar{\sigma} = e n_0 \lambda_D$.

186 The numerical simulations are performed using periodic boundary conditions in phys-
187 ical space and assuming electron and ion distribution functions equal to zero for veloc-
188 ities outside the given velocity range (i.e. $f_e(x, |v_e| > v_{e,max}, t) = 0$ and $f_p(x, |v_i| > v_{i,max}, t) =$
189 0). Table C1 and Table C2 list the simulation parameters.

190 The simulations are initialized with uniform single Maxwellian distribution func-
191 tions for ions and shifted Maxwellian distribution functions for the electrons to minimize
192 transient effects. Such initialization is discussed in Appendix A. Transient signals will
193 be investigated in a future dedicated work and are out of the scope of this study.

194 Each emitting antenna is modeled as the external source $\rho_{ext.}(x, t) = \sigma(t)\delta(x)$ char-
195 acterized by the following oscillating charge term:

$$196 \quad \sigma(t) = \sigma_0 \sin(\omega t) \quad (3)$$

197 where σ is the oscillating charge per unit surface, σ_0 is the amplitude of the oscillating
198 charge, $\omega = 2\pi f$ is the angular frequency with f the emission frequency. Each of our
199 1D antennas is equivalent in 3D space to an oscillating, uniformly charged, infinite plan-
200 ar grid. Such a grid is supposed to be so thin that the collection of particles at its sur-
201 face is negligible, resulting in particles moving freely across the antennas. This choice,
202 also adopted in previous studies (Buckley, 1968), allows one to neglect the collection of
203 electrons and ions from the emitting antenna. Each external antenna generates an os-
204 cillating electric signal composed of one uniform term (hereafter called far-field term)
205 and a spatially damped term that propagates to the surrounding plasma from the po-
206 sition of the antenna (hereafter called close-field term) (Podesta, 2005). The far-field term
207 corresponds to the electric field expected for the cold plasma limit (Chasseriaux et al.,
208 1972) (i.e. $\omega \gg \omega_p$), while the close-field term represents the wave-component of the
209 perturbation generated by the emitting antennas. Periodic boundary conditions on the
210 simulation box require the use of, at least, two antennas of opposite oscillating charges.
211 This configuration is equivalent to that of an oscillating capacitor, composed of two par-
212 allel infinite charged planes embedded in the plasma. Such capacitor perturbs the sur-
213 rounding plasma with an electric field that is the sum of (i) a spatially constant far-field
214 term and (ii) close-field terms propagating in-between the two electrodes.

215 In our 1D model, the far-field term is equivalent, in 3D, to the electric field compo-
216 nent that would decrease in $d_{ph.}^{-2}$ with the distance, $d_{ph.}$, from a point source emitting
217 antenna. The close-field term is equivalent in 3D to the radial component of the wave

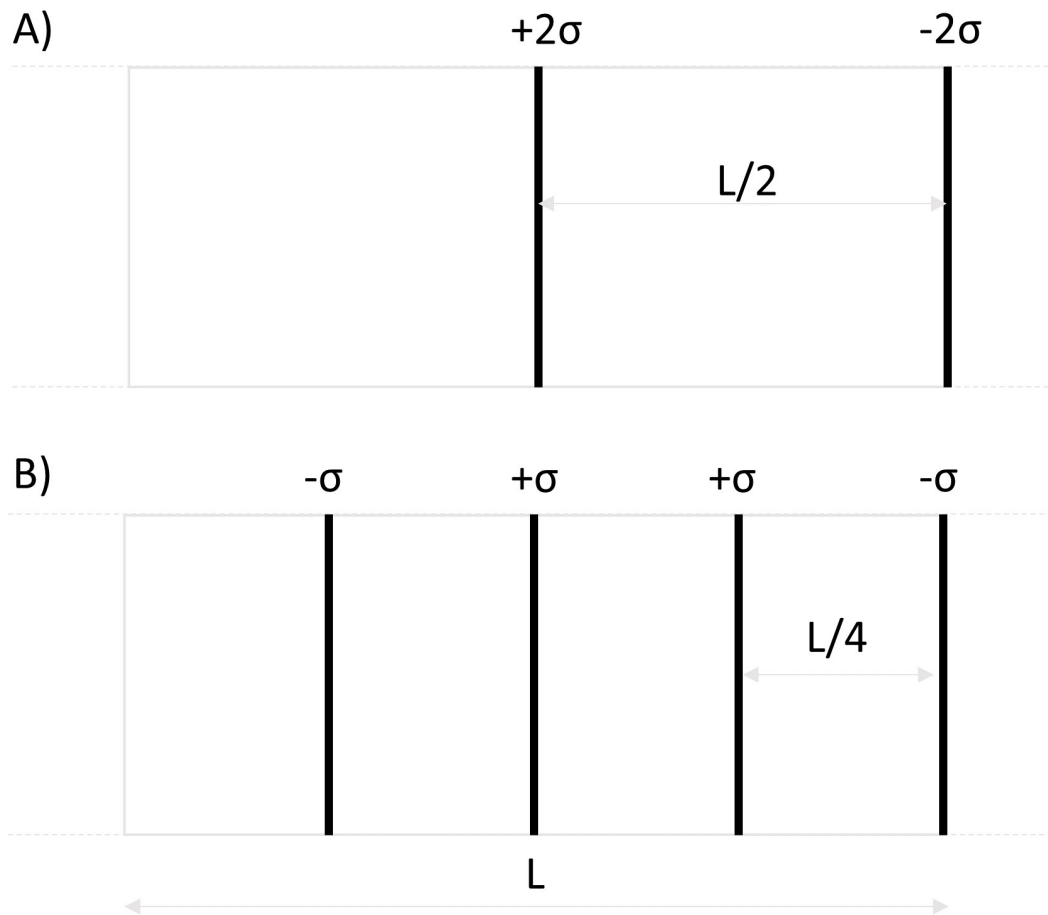


Figure 1. Representation of the emitting antennas configuration in the periodic simulation box. The top (resp. bottom) panel represents the model A (resp. B), characterized by two (resp. four) emitting antennas.

218 that would propagate from the same emitting point source antenna to the surrounding
 219 plasma. We note that in 1D the amplitude of the electric field oscillations at large dis-
 220 tances from the emitting antennas is overestimated w.r.t. that expected in 3D due to
 221 the far-field term. In order to account for this 1D artifact, we use in our study two dif-
 222 ferent antennas configurations, hereafter called model A and model B (top and bottom
 223 panel of Figure 1).

224 Model A is optimized for the investigation of the non-linear effects triggered in the
 225 plasma by the MI emission signal. In particular, it benefits from the presence of the 1D
 226 artifact term: enhanced electric field fluctuation amplitudes correspond to enhanced growth-
 227 rate of the generated non-linear plasma perturbations. Thus, the simulation durations
 228 needed to study non-linear plasma perturbations are reduced. For this model, the po-
 229 sitions of the emitting capacitor plates are chosen in order to maximize the distance be-
 230 tween any two opposite charge electrodes. Practically, this is done by imposing the dis-
 231 tance between the electrodes (represented as vertical lines in top panel of Figure 1) of
 232 each capacitor as half the length of the numerical spatial box and by superposing, for
 233 any two neighboring capacitors, the antennas that emit the same electric signal.

234 Model B is optimized for the quantitative investigation of MI diagnostic performance.
 235 It is devised to obtain MI spectra that either consider or neglect the effects of the 1D
 236 artifact depending on the position in the simulation box at which the electric fluctua-
 237 tions are retrieved. We consider (resp. neglect) the effects of the 1D electric-field arti-
 238 fact term by analyzing the electric oscillations generated in the plasma between two op-
 239 posite (resp. same) charge antennas, where the far-field component is doubled (resp. can-
 240 celled out). The positions of the antennas in the numerical box are chosen to maximize
 241 both the distance between neighboring capacitors and the distance between the plates
 242 of each capacitor. Practically, for this model, any two emitting antennas are separated
 243 by a distance equal to a quarter of the numerical spatial box length. This model allows
 244 one to investigate what non-linear effects are triggered by the close-field and far-field terms
 245 separately.

246 Since the contribution of the far-field term is always present in 3D experimental
 247 MI spectra, for consistency with 3D MI experimental measurements, in this document
 248 we only discuss the plasma density and electron temperature obtained *including* such
 249 contribution. In the following, the plasma density and the electron temperature are ob-
 250 tained by applying the same data analysis techniques used for the investigation of ex-
 251 perimental MI spectra (Gilet et al., 2017; Wattieaux et al., 2020).

252 3 Non-linear Effects Generated in an Unmagnetized Space Plasma Ex- 253 cited by an External Large Amplitude Oscillating Antenna.

254 In this section we investigate the impact of moderate to strong electric antenna emis-
 255 sion at a given frequency on the nearby perturbed plasma.

256 We define the electric-to-thermal energy ratio $\alpha = (E^2 \epsilon_0) / (n_0 k_b T_e)$ as the param-
 257 eter identifying the level of non-linearity associated to the electric field E , driven by the
 258 antenna emission. This ratio depends on the amplitude and on the frequency of the os-
 259 cillating electric potential at the antenna. In particular, the electric field that propagates
 260 in the plasma scales with frequency ω as the inverse of the collisionless unmagnetized
 261 cold plasma dielectric permittivity, corresponding to $(1 - \omega_p^2 / \omega^2)^{-1}$ (Podesta, 2005) for
 262 $\omega \geq \omega_p$. In order to model different levels of α that can be achieved in MI experiments,
 263 we compare a number of simulations made using different frequencies but with same emis-
 264 sion amplitudes.

265 The numerical simulations are set on the typical timescale of experimental MI emis-
 266 sion durations, which turns out to be of the order of $N = 15$ oscillation periods of the
 267 emitted frequency. As a consequence, we neglect all effects that would develop over larger
 268 timescales. The total simulation time, the size of the physical box, the velocity range over

269 which the ion and electron distribution functions are defined, as well as all other most
270 relevant parameters are listed in Table C1.

271 In the following, we investigate with Model A i) the non-linear perturbations trig-
272 gered by single frequency emissions with a fixed ion background (section 3.1) and ii) the
273 impact of the ion dynamics on the perturbation evolution (section 3.2).

274 3.1 Large Amplitude Perturbations of the Plasma Dielectric with Fixed 275 Ions

276 In this section we consider the case of a fixed neutralizing background of ions and
277 focus on the electron dynamics only. In particular, we investigate the plasma response
278 to electric signals generated by an oscillating charge with amplitude $\sigma = 0.1\bar{\sigma}$ at three
279 different frequencies: $0.5\omega_p$ (simulation NF_01), $1.1\omega_p$ (simulation NF_02) or $2.0\omega_p$ (sim-
280 ulation NF_03). The corresponding electric-to-thermal energy ratios are: 0.01, 0.33, 0.01.

281 On the one hand, for antenna emissions at $0.5\omega_p$ and $2.0\omega_p$, the electric perturba-
282 tion that propagates in the plasma oscillates at the emission frequency. However, the per-
283 turbation is limited to regions close to the antennas, because it corresponds either to an
284 evanescent wave (for $0.5\omega_p$) or to a propagating wave affected by strong Landau damp-
285 ing (for $2.0\omega_p$) (Brunetti et al., 2000) as consistent with a linear plasma response. In both
286 cases, we do not observe any non-linear effect.

287 On the other hand, at frequency $\omega = 1.1\omega_p$ corresponding to wavenumber $k_L =$
288 $0.244 \lambda_D^{-1}$, a non-linear plasma response occurs because of the conversion efficiency nearby
289 the plasma frequency. The signature of this wave-wave interaction is shown in the charge
290 density Fourier spectrum in Figure 2, where the black dashed lines indicate the emitted
291 Langmuir wave at (k_L, ω_L) and the red line indicates the dispersion relation of Langmuir
292 waves $\omega_L^2/\omega_p^2 = 1 + 3\lambda_D^2 k_L^2$.

293 First, on top of the emitted Langmuir wave, we also observe the so-called virtual
294 wave at $(2k_L, 2\omega_L)$ (Dysthe & Franklin, 1970) which is represented as a localized increase
295 in charge density at position $(k_R = -0.488 \lambda_D^{-1}, \omega = 2.2\omega_p)$ of Figure 2. Second, sig-
296 natures of wave-particle interactions are observed. At the early stage of the simulations
297 ($t \simeq 20\omega_p^{-1}$) we observe an efficient acceleration of the electrons pushed by the wave
298 electric field and eventually propagating ballistically. In the (x, v_x) phase space domain,
299 this process corresponds to the formation of finger-like filaments on the distribution func-
300 tion, as shown for the electron distribution function represented in top panel of Figure 3
301 between $v_e = 2v_{the}$ and $v_e = 7v_{the}$, at positions $[20\lambda_D - 50\lambda_D]$, $[30\lambda_D - 90\lambda_D]$ and
302 $[50\lambda_D - 130\lambda_D]$. We note that given the Langmuir wave packet propagating at group
303 velocity $v_g = 0.67v_{the}$, the distance covered by the emitted wave packet in the plasma
304 at $t \simeq 20\omega_p^{-1}$ is about $13\lambda_D$. At a later stage of the simulations ($t \simeq 120\omega_p^{-1}$), the res-
305 onant electrons moving at nearly the phase velocity of the wave have been eventually trapped
306 by the wave potential. This process leads to the formation of vortex-like structures in
307 phase space. Such structures are visible in Figure 4 top panel at velocities near $v_\phi \simeq$
308 $4.5v_{the}$ which is the phase velocity of the emitted wave. We note that the Landau damp-
309 ing of the wave-packet does not affect the growth time rate of this trapping process, be-
310 cause the perturbing signal is *continuously* excited by the antenna emission. The oscil-
311 lation period of these trapped electrons is $T_B = \sqrt{m_e}/(eEk)$ (Zakharov & Karpman,
312 1963; O’Neil, 1965). As expected, the trapping process starts nearby the emitting an-
313 tenna, leading to nearly formed vortexes in phase space when the wave-packet propa-
314 gating in the plasma reaches distance $L_v \simeq T_B v_\phi$. As the wave packet moves at group
315 velocity v_g , no trapping is expected on timescales smaller than an *efficient* trapping time
316 $t_{trap} \simeq L_v/v_g = T_B v_\phi/v_g = T_B(1 - \omega_p^2/\omega^2)^{-1} \gg T_B$. In the numerical experiment de-
317 scribed in this section, we find $T_B \simeq 17\omega_p^{-1}$, for which vortexes in phase space form at
318 a distance $L_v \simeq 75\lambda_D$ from the emitting antenna, starting from the *efficient* trapping
319 time $t_{trap} \geq 113\omega_p^{-1}$. The above analysis is strongly limited by the fixed ions assump-

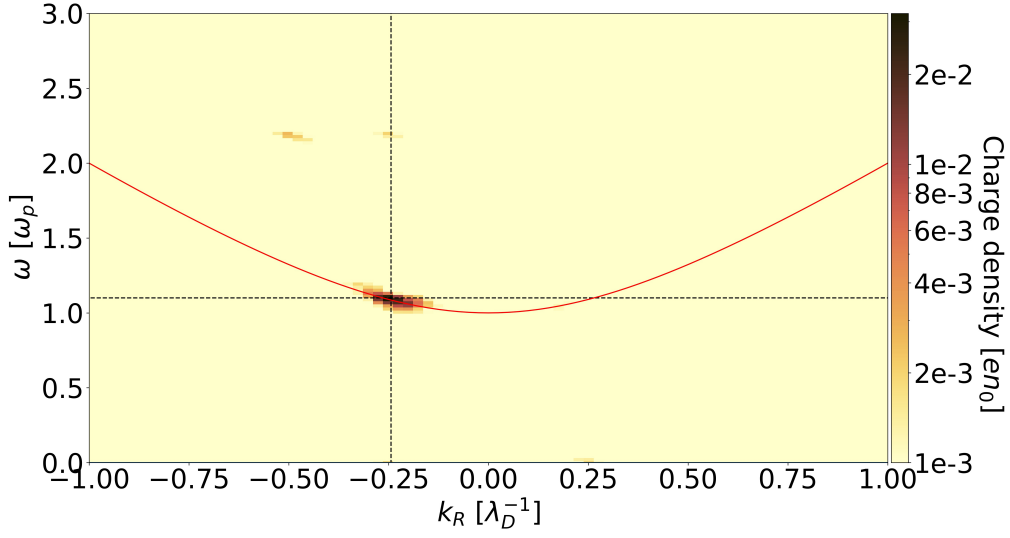


Figure 2. Charge density Fourier spectrum, in the real wavenumber-frequency space (k_R, ω), for simulation NF_01. The horizontal and vertical dotted black lines indicate the Langmuir wave at the antenna emission frequency ($-k_L, \omega_L$). The Langmuir wave dispersion relation is shown as a red solid line.

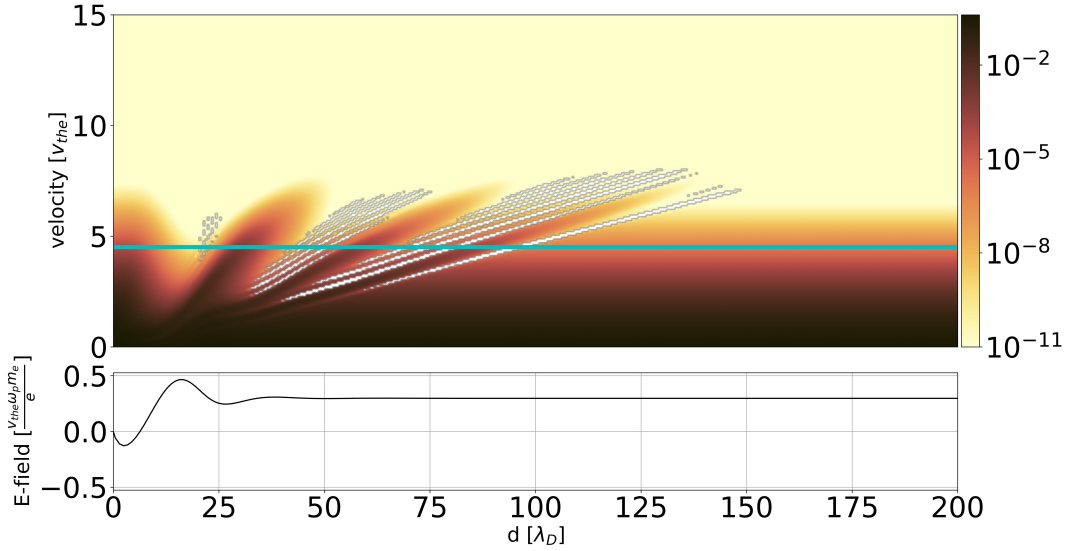


Figure 3. Efficient acceleration of electrons in regions close to the emitting antenna. Top panel: electron velocity distribution function in phase space; the blue line represents the phase velocity of the emitted Langmuir wave, for simulation NF_02 (emission frequency $\omega = 1.1\omega_p$) at time $t \simeq 20\omega_p^{-1}$. Bottom panel: corresponding electric field in the plasma, as a function of distance d from the emitting antenna, located at $d = 0$.

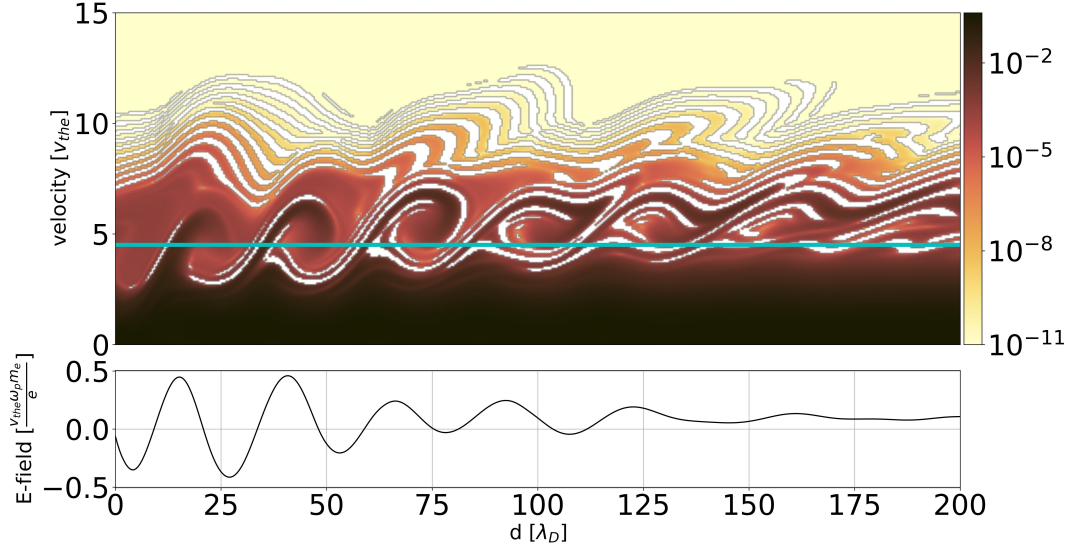


Figure 4. Signatures of particles trapping in phase space. Same as Figure 3 at time $t \simeq 120\omega_p^{-1}$.

tion to times shorter than the ion inertial time ($\sim m_i/m_e$ in dimensionless units) (Califano et al., 2007). This assumption is relaxed in the next section.

3.2 Large Amplitude Perturbations of the Plasma Dielectric for Moving Ions

In this section, we investigate the influence of the ion dynamics on the propagation of an antenna emitted oscillating electric potential by adding the ion Vlasov equation to the previous electron Vlasov-Poisson system (equation 1 and equation 2). We use an ion-to-electron mass ratio $m_i/m_e = 100$ and an ion-to-electron temperature ratio $T_i/T_e = 0.1$. We consider a reduced mass ratio for computational reasons, while the temperature ratio is chosen to enable ion acoustic fluctuations to propagate.

We initialize the simulations with the same setup as in the fixed background limit discussed in section 3.1. The investigated emission frequencies are $0.5 \omega_p$ (simulation NI_01), $1.1 \omega_p$ (simulation NI_02) and $2.0 \omega_p$ (simulation NI_03), emission amplitude fixed to $\sigma = 0.1 en_0 \lambda_D$. The corresponding electric-to-thermal energy ratio in the plasma is 0.01, 0.33 and 0.01, respectively.

At the emission frequencies of $0.5 \omega_p$ and $2.0 \omega_p$, the ion dynamics does not modify the propagation of the electric field in the plasma, as expected since no non-linear perturbations are observed (section 3.1). The results (not shown here) are identical to those reported with fixed ions.

On the contrary, at emission frequency $\omega = 1.1 \omega_p$, the ion dynamics strongly impacts the electric fluctuation propagating as a Langmuir wave at frequency $\omega_L = \omega$. Similarly to the model with fixed ions, we observe (i) ballistic electrons initially accelerated by the electric field escaping the wave packet, (ii) wave-particle interaction signatures as phase space vortices at the phase velocity of the emitted wave, (iii) so-called virtual waves excited at $(-2k_L, 2\omega_L)$. On top of this, we also observe new signatures associated to the ion motion. Such signatures are shown in the ion (resp. charge) density Fourier spectrum in the bottom (resp. top) panel of Figure 5.

347 First, ion density oscillations show that ions are accelerated at the wavefront of the
 348 propagating Langmuir wave packet, resulting in the generation of ion acoustic oscillations
 349 propagating both forward and backward w.r.t. the Langmuir wave packet front (not
 350 shown here). The signature corresponding to these ion acoustic waves (IAW) is observed
 351 at $(\pm k_L, \omega_{IAW})$ in the Fourier space of the ion charge density (bottom panel of Figure 5),
 352 where $k_L = 0.244\lambda_D$ is the wavenumber of the excited Langmuir wave and $\omega_{IAW} = 0.025\omega_p$
 353 is the corresponding IAW oscillation frequency. Such frequency is obtained from the IAW
 354 dispersion relation $\omega_{IAW}^2 = (k_{IAW}^2 C_s^2)/(1+k_{IAW}^2 \lambda_D^2)$ with C_s the ion sound-speed. Note
 355 that these ion acoustic modes do not correspond to what one would expect in the case
 356 of parametric excitation processes. In that case, as three waves interaction processes are
 357 triggered, the energy of the emitted Langmuir wave ($k_L = -0.244\lambda_D^{-1}$, $\omega_L = 1.1\omega_p$)
 358 would excite wave pairs respecting the resonant relations (Dysthe & Franklin, 1970) $\omega_L =$
 359 $\omega_1 + \omega_2$ and $k_L = k_1 + k_2$, where (k_1, ω_1) and (k_2, ω_2) are modes of the system. The
 360 generation of these ion acoustic perturbations is attributed to the ponderomotive force
 361 (Califano & Lontano, 1999; Henri et al., 2011) triggered by the strong electric energy gra-
 362 dient at the front of the Langmuir wave packet that acts as an equivalent pressure gra-
 363 dient on the ions. By performing a series of secondary simulations with larger ion-to-electron
 364 temperature ratios (i.e. $T_i/T_e \simeq 1$), we observed that such IAWs vanish directly after
 365 being generated at the wave-front of the propagating Langmuir wave due to their sig-
 366 nificant damping rate.

367 Second, large ion acoustic density oscillations $\Delta n_i/n_i$ reflect the emitted forward
 368 Langmuir wave ($-k_L = -0.244\lambda_D^{-1}$, $\omega_L = 1.1\omega_p$) into a backward Langmuir wave ($k_L =$
 369 $0.244\lambda_D^{-1}$, $\omega_L = 1.1\omega_p$) (Tkachenko et al., 2021). This effect is equivalent to the iono-
 370 spheric reflection of radio waves. With an emission frequency $\omega = 1.1\omega_p$, the Langmuir
 371 wave reflection occurs only in regions where ion density oscillations exceed $\Delta n_i/n_i >$
 372 0.2 , as confirmed by our simulations. Third, non-linear beats of the ion acoustic wave
 373 at $(\pm k_L = \pm 0.244\lambda_D^{-1}$, $\omega_{IAW} = 0.025\omega_p)$ trigger ion oscillations at the harmonic $(\pm 2k_L =$
 374 $\pm 0.488\lambda_D^{-1}$, $2\omega_{IAW} = 0.05\omega_p)$, corresponding to the signature of localized charge den-
 375 sity observed at that position in bottom panel of Figure 5. At later stages of the simu-
 376 lations, IAWs at the second harmonic $(3k_L, 3\omega_{IAW})$ resulting from the non-linear in-
 377 teraction between (k_L, ω_{IAW}) and $(2k_L, 2\omega_{IAW})$ are also observed in ion density oscil-
 378 lations (Figure 5 bottom panel). On top of that, virtual waves are observed at $(2k_L, \omega +$
 379 $\omega_{IAW})$ (Figure 5 top panel) as a result of the interaction between (k_L, ω) and (k_L, ω_{IAW}) .
 380 The non-linear interactions described in this section have been identified in three steps.
 381 First, we investigated the time evolution of the energy location within the frequency-wavenumber
 382 domain. Second, we identified the resonant relations between wave triads. Third, we iso-
 383 lated the wave packets associated to each resonant mode by filtering them in Fourier space.
 384 Practically, this consists of isolating within the frequency-wavenumber domain each mode
 385 of interest and converting it back to time-space domain. By doing so, we have identi-
 386 fied the location of the wave packets in physical space and confirmed at which time and
 387 location each identified three-wave interaction occurred. In this analysis, we have con-
 388 centrated on three-wave interactions, associated to quadratic interactions, i.e. the lower-
 389 order non-linear interactions in this model. We have also verified that higher order non-
 390 linear interactions are negligible in our simulations.

391 We conclude this section by emphasizing the necessity to self-consistently model
 392 the coupled electron and ion dynamics. This is particularly needed when targeting fi-
 393 nite amplitude plasma oscillations at frequencies close to the plasma frequency, for which
 394 plasma non-linearities triggered by significant electric-to-thermal energy ratios come into
 395 play. Our simulations show that neglecting the ion motion results to a significant un-
 396 derestimation of the non-linear plasma interactions triggered by the instrument. When
 397 the ion motion is also modelled, ion acoustic waves can be triggered. This opens new chan-
 398 nels for energy transfer from the emission frequency towards other frequencies, with an
 399 energy transfer that depends on both the emission frequency and the emission duration.
 400 This points out the need to self-consistently model both the electron and the ion dynam-

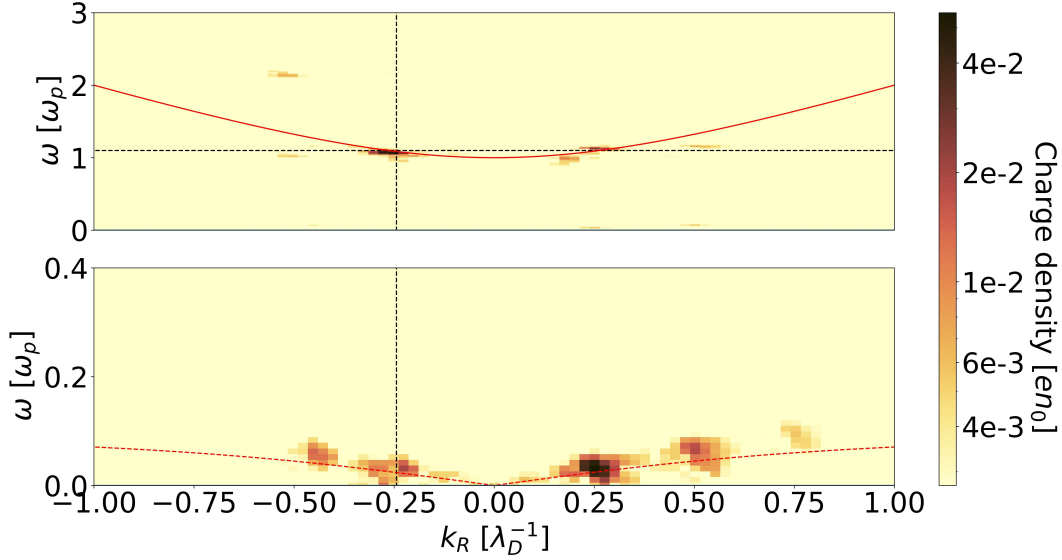


Figure 5. Charge and ion density Fourier spectra. Both top and bottom panel refer to simulation NI_02 (emission frequency $\omega = 1.1\omega_p$). Top panel: 2D Fourier transform of the net charge density, up to time $550\omega_p^{-1}$. The red solid line represents the Langmuir waves dispersion relation. The black dotted lines represent the ω_L and k_L of the emitted plasma wave. Bottom panel: 2D Fourier transform of the ion density, up to time $550\omega_p^{-1}$. The red dotted line represents the IAW waves dispersion relation. The black dotted line represents the k_L of the emitted plasma wave.

ics when addressing the modeling and diagnostic performance of large MI emission amplitude likely to trigger non-linear plasma dynamics.

4 Significance for In Situ Density and Temperature Diagnostics Performed in Space Plasmas by Mutual Impedance Experiments

In this section, we quantify the consequences of the non-linear dynamics described in the previous section 3 on the instrumental performance of MI experiments in space plasma diagnostics, focusing on in situ plasma density and electron temperature measurements. This objective is achieved by comparing and analyzing MI spectra modeled for both linear or non-linear responses of the diagnosed plasma. For this purpose, we simulate MI spectra obtained for electric antenna emissions ranging over electric-to-thermal energy ratio from 10^{-10} to 1. Note that we hereby define the electric-to-thermal energy ratio corresponding to each MI spectra as the energy ratio obtained for emission frequencies $\omega \gg \omega_p$. This choice is made to avoid any confusion associated to the frequency dependency of the electric potential oscillations in the plasma, during a MI frequency sweep, previously discussed in section 3. In our analysis, we include the ions' dynamics, using an ion-to-electron mass ratio $m_i/m_e = 100$ (discussed in section 4.5) and an ion-to-electron temperature ratio $T_i/T_e = 0.1$.

Note that the MI diagnostic technique used in experimental space applications is based on retrieving plasma parameters, such as the plasma density and electron temperature, from the shape of the MI spectra because it itself strongly depends on the *linear* plasma dielectric. This instrumental technique is therefore essentially based on the assumption of a *linear* response of the diagnosed plasma to the emitted electric perturbation. Practically, a linear plasma behavior is assumed when deriving plasma parameters using the MI diagnostic technique. From an instrumental point of view, whatever *non-*

linear effect resulting from this emitted electric perturbation which would impact the shape of the MI spectra is therefore to be considered as spurious. Small perturbations of the plasma dielectric (i.e. a *quasi-linear* response of the diagnosed plasma) might be acceptable, from an instrumental point of view, as long as the resulting MI spectra does not differ much from the one expected in a linear case. For the above-mentioned reason, we also consider in this study a linear plasma response to the MI external electric excitation, in order to mimic typical experimental MI data analysis dedicated to the determination of both the plasma density and electron temperature. A linear plasma response is always assumed, even for plasma oscillations generated from significant antenna emission amplitudes for which *non-linear* perturbations of the plasma are occurring. The consequences of these *non-linear* plasma perturbations on the MI spectra might lead to a discrepancy between the *apparent* plasma density and electron temperature and the *actual* density and temperature. From the discrepancy between the *apparent* and the *actual* plasma parameters, we compute a diagnostic error, from which we derive the performance and robustness of the MI measurement technique. In particular, with this approach, we assess quantitatively the errors made in typical MI experiments when using data treatment techniques conceived for *linear* plasma perturbations to analyze MI spectra obtained for a *non-linear* plasma response.

4.1 Synthetic Mutual Impedance Spectra

MI spectra are built from the plasma response to MI emissions. A MI emitting electric antenna with oscillating electric signals of known amplitude A and frequency ω perturbs the plasma. *Simultaneously*, receiving electric antennas measure the electric potential fluctuations that have propagated in the diagnosed plasma, at the same frequency ω . The total duration of the emission signal is $t_\omega = NT_\omega$, where $T_\omega = 2\pi/\omega$ is the oscillation period and the amount of repetitions is chosen $N = 15$ in this work. This choice is consistent with the typical instrumental design of MI instruments. Practically, MI experiments successively scan one frequency after the other within a predefined frequency range of interest, to perform a MI frequency sweep. In our numerical experiments, we however choose to perform separate simulations for each emitted frequency. Therefore, we neglect any possible coupling between what would be successive emitted frequencies of a MI frequency sweep. In doing so, we assume that the waiting time between two successive emissions is sufficient for the plasma to relax back to its unperturbed state. This choice is discussed in section 4.4.

Mimicking experimental MI applications, we investigate MI frequency sweeps characterized by a relative frequency resolution $\Delta\omega/\omega = 5\%$, that corresponds to a relative density resolution of $\Delta n_e/n_e = 10\%$. Such resolution is consistent with that used in recent MI experiments, such as the DFP-COMPLIMENT experiment of the ESA Comet Interceptor mission. This investigation is performed using model B, considering the contribution of the far-field term (described in section 2). The list of settings parameter defining the simulations from which MI spectra are built is shown in Table C2.

Using a dipolar reception antenna configuration, MI spectra are built from the electric potential oscillation difference measured between two electric antennas located at distance d and $2d$ from the emitting antenna, with d ranging from $5\lambda_D$ to $40\lambda_D$. These distances between the emission and reception antennas correspond to the typical MI experiment emitting-receiving antennas distances in previous and forthcoming space missions (Rosetta RPC-MIP, BepiColombo PWI/AM2P, JUICE RPWI/MIME, Comet Interceptor DFP-COMPLIMENT).

From the electric potential oscillations obtained in our numerical simulations, synthetic MI spectra are built using the following procedure.

(i) First, we apply signal apodization to the electric potential oscillations. In this study, we adopted the Hann window, the same apodization technique currently adopted

476 for the on-board analysis of MI measurements in previous space applications, such as RPC-
477 MIP on Rosetta, AM2P on BepiColombo and MIME on JUICE.

478 (ii) Second, we compute, at the emission frequency ω , the amplitude of the signal
479 from a Discrete Fourier Transform of this windowed time series. We repeat this process
480 for each emitted single frequency to obtain a spectrum.

481 (iii) Third, the obtained spectrum is normalized by the offset introduced by the Hann
482 window, in order to correct for the apodization.

483 (iv) Finally, the resulting spectrum is normalized by the corresponding MI spec-
484 trum obtained in vacuum, a procedure usually performed with MI experiments (Henri
485 et al., 2017). Indeed, under a linear plasma response assumption, this normalized MI spec-
486 trum is independent of the antenna emission amplitude. Therefore, this normalization
487 procedure ensures an unbiased comparison between spectra obtained for different electric-
488 to-thermal energy ratios. The resulting normalized MI spectrum is expressed in decibel
489 scale, where the reference amplitude is that obtained for vacuum conditions.

490 For this investigation, we assume negligible perturbations of MI spectra related to
491 noise. This assumption is not valid for experimental space applications, where the in-
492 fluence of *instrumental noise* on MI measurements is, at times, significant. The *instru-*
493 *mental noise*, related to the electronics of the MI instrument, affects the accuracy of the
494 measurements. Typically, it affects experimental MI spectra with perturbations of the
495 order of $1dB$ and therefore, in order to mimic MI experimental space applications, we
496 discard all perturbations of MI spectra up to $1dB$.

497 We have shown in section 3.1 and section 3.2 that it is necessary to model both the
498 electron and ion dynamics when investigating the propagation and evolution of finite am-
499 plitude waves associated to large amplitude emissions. We now illustrate (Figure 6) to
500 what extent discarding the ion dynamics impacts MI measurements. We compare two
501 MI spectra obtained either modeling (violet line) or neglecting (blue line) the motion of
502 ions. Both spectra are computed at distance $d = 5\lambda_D$ from the emitting antennas and
503 $\alpha = 0.6$ for which significant non-linear plasma interactions are expected. We note that
504 the contribution of the ion dynamics significantly modifies the resonant shape of the spec-
505 tra. In particular, we find differences up to 7 dB, which is well above the typical instru-
506 mental noise of MI measurements.

507 Therefore, in the rest of this work, we shall only consider numerical simulations that
508 include both the electron and ion dynamics when investigating MI spectra. We now con-
509 centrate on the impact of finite amplitude emissions on mutual impedance spectra.

510 Examples of synthetic MI spectra are shown in Figure 7, for different electric-to-
511 thermal energy ratios, for the emitting-receiving antennas distances $d \simeq 5\lambda_D$, $d \simeq 10\lambda_D$
512 and $d \simeq 20\lambda_D$, from top to bottom panels.

513 On the one hand, we observe that the MI synthetic spectra obtained for electric-
514 to-thermal energy ratios $\alpha \leq 10^{-2}$ (corresponding to simulations SI1_01 to SI1_14)
515 and represented as a light blue line are essentially identical (within the typical *instru-*
516 *mental noise* levels) to the linear spectra (corresponding to simulations SL_01 to SL_48)
517 obtained for $\alpha = 10^{-10}$ and represented as a blue line.

518 On the other hand, when $\alpha > 10^{-2}$ (i.e. from simulations SI2_01 to SI2_14, SI3_01
519 to SI3_14 and SI4_01 to SI4_14), we observe instead significant differences between the
520 associated spectra (i.e. orange, red and green lines) and the reference spectra (blue line),
521 especially at frequencies close to the plasma frequency for spectra obtained at $d \leq 20\lambda_D$.
522 The discrepancies observed at frequencies close to the plasma frequency are consistent
523 with the results of section 3.2, where we have shown that the plasma is non-linearly per-
524 turbed by finite amplitude antenna emissions at frequency close to the plasma frequency
525 ($\omega = 1.1\omega_p$). Note that, the discrepancies that we found exceeding typical *instru-*
526 *mental noise* levels are expected to be measurable in the case of experimental space appli-
527 cations for significant antenna emission amplitudes.

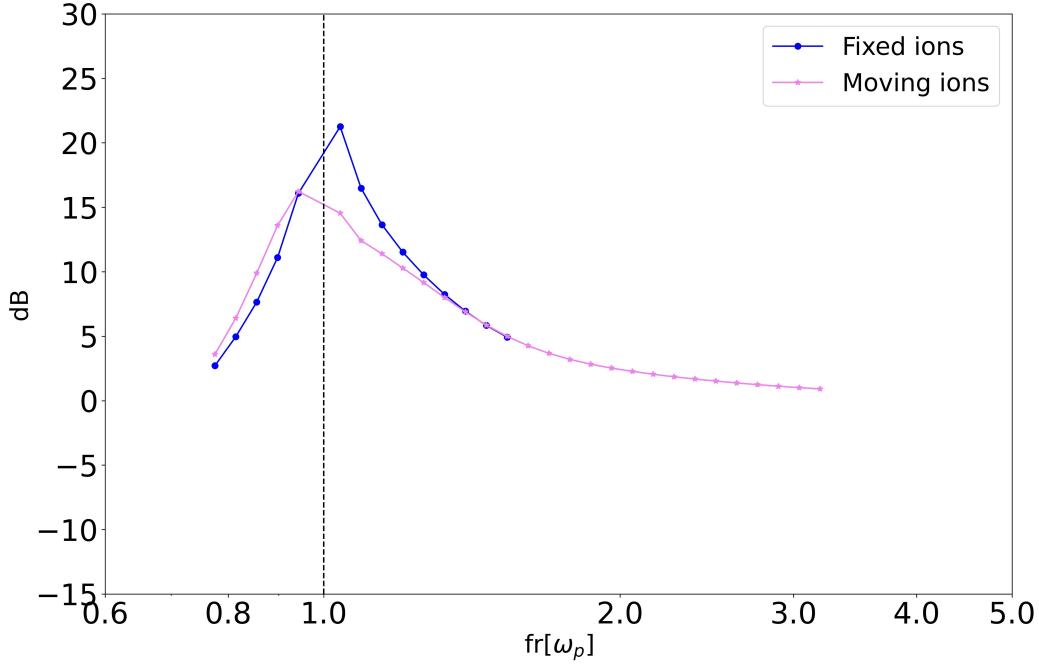


Figure 6. Mutual impedance spectra obtain with immobile (blue) and mobile (violet) ions. Both spectra are obtained for $\alpha = 0.6$ at distance $d = 5\lambda_D$ from the emitting antenna.

528 What is the expected trend of MI spectra disturbed by non-linear plasma pertur-
 529 bations induced by the finite amplitude antenna emission, compared to the undisturbed
 530 MI spectra associated to a linear plasma response?

531 The analysis performed in section 3.2 suggests that the MI spectra, built from the
 532 electric oscillation measured in the plasma at the emission frequencies, should be affected
 533 by two counteracting phenomena, triggered by the finite amplitude antenna emission.
 534 On the one hand, non-linear wave-wave interactions open energy channels that redistribute
 535 the energy at frequencies different from the emission frequency. This results in a net *de-*
 536 *crease* in the received (normalized) MI amplitude at the emission frequency, compared
 537 to the received (normalized) amplitude that would be measured in the linear case. On
 538 the other hand, wave-particle interactions also result in a non-linear feedback on the plasma
 539 distribution function (plateauing in velocity space) that decreases, or can even suppress,
 540 the spatial damping of the emitted wave packet. Note worthily, under a linear plasma
 541 response assumption, the MI spectra at frequencies above, and close to, the plasma fre-
 542 quency are strongly shaped by the spatial Landau damping of the Langmuir wave ex-
 543 cited in the plasma by the emission antenna. Therefore, wave-particle interactions im-
 544 ply a net *increase* in the received (normalized) MI amplitude at the emission frequency,
 545 compared to the received (normalized) amplitude that would be measured in the linear
 546 case.

547 Because of these two counteracting phenomena, it is not straightforward to know
 548 the actual shape of the MI spectra close to the resonant frequency (in this study, the plasma
 549 frequency), hence the need for numerical simulations. For instance, in the specific con-
 550 ditions considered in this section (i.e. with antenna distances of $d \simeq 5\lambda_D$, $d \simeq 10\lambda_D$
 551 and $d \simeq 20\lambda_D$), we find a maximum discrepancy between the MI synthetic spectra per-
 552 turbed by non-linear plasma effects (e.g. green solid line in Figure 7) and the reference
 553 linear MI synthetic spectra (blue solid line in Figure 7) at the resonance peak of about
 554 10dB. This spectrally localized, but significant, discrepancy is well above the typical in-

555 instrumental noise of MI instruments (e.g. 1dB): we therefore expect such perturbations
 556 to actually be measurable, and possibly even dominant, for MI spectra obtained in low
 557 temperature space plasmas. It is therefore legitimate to assess quantitatively the impact
 558 of these "spurious" (from an instrumental diagnostic point of view) non-linear plasma
 559 perturbations of the MI spectra on plasma density and electron temperature measure-
 560 ments performance when using the MI diagnostic technique.

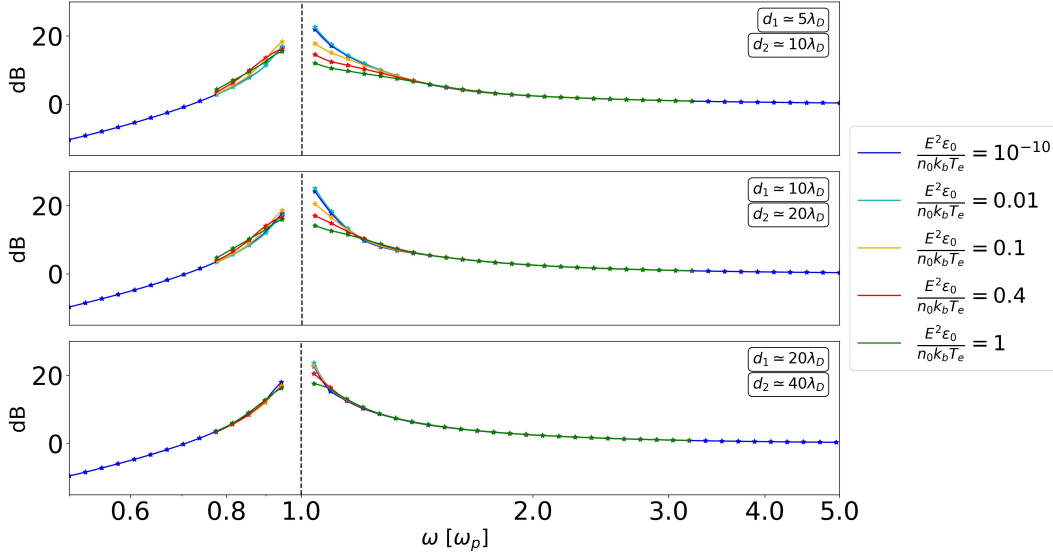


Figure 7. Mutual impedance spectra. The distances of the two receiving antennas from the emitting antenna are represented as d_1 and $d_2 = 2d_1$. From top to bottom panel, mutual impedance spectra are obtained for $d_1 \simeq 5\lambda_D$, $d_1 \simeq 10\lambda_D$, $d_1 \simeq 20\lambda_D$, for different antenna emission amplitudes (solid lines).

561 We describe in the following sections the procedure used to derive the plasma density
 562 (section 4.2) and electron temperature (section 4.3) from the normalized MI spectra,
 563 expressed in dB.

564 4.2 Plasma Density Diagnostic Performance for Strong Amplitude Emis- 565 sions

566 We here focus on evaluating the plasma density diagnostic performance of MI ex-
 567 periments for finite amplitude antenna electric emissions likely to trigger non-linear ef-
 568 fects in the diagnosed plasma. We do so in two steps. First, for each spectrum we es-
 569 timate the plasma frequency (hereafter called *apparent* plasma frequency, $\omega_{p,app.}$). Sec-
 570 ond, we compute the plasma frequency relative error by comparing the apparent plasma
 571 frequency to the (known) *actual* plasma frequency (ω_p) of the spectrum as follows:

$$572 \frac{\Delta\omega_{p,app.}}{\omega_p} = \frac{\|\omega_{p,app.} - \omega_p\|}{\omega_p} \quad (4)$$

573 The MI plasma density diagnostic performance is then obtained by converting the plasma
 574 frequency relative error to plasma density relative error:

$$575 \frac{\Delta n_{e,app.}}{n_e} = \frac{\|n_{e,app.} - n_e\|}{n_e} = 2 \frac{\Delta\omega_{p,app.}}{\omega_p} \quad (5)$$

576 The considered frequency resolution of $\Delta\omega/\omega = 5\%$ corresponds to a plasma density
 577 resolution $\Delta n_e/n_e = 10\%$. We consider that MI experiment is robust against strong
 578 antenna amplitude emissions if the plasma density relative error is below this uncertainty.

579 We evaluate the plasma density diagnostic performance for antenna emission am-
 580 plitudes corresponding to electric-to-thermal energy ratios $\alpha \in (10^{-10}, 1)$ (top to bot-
 581 tom panels of Figure 8), in function of the emitting-receiving antennas distance d rang-
 582 ing from $5\lambda_D$ to $40\lambda_D$.

583 The apparent plasma frequency is identified from MI spectra as the frequency cor-
 584 responding to the position of the resonant peak signature in the spectra (Storey et al.,
 585 1969; Béghin & Debrie, 1972; Rooy et al., 1972; Pottelette et al., 1975; Décréau et al.,
 586 1978; Pottelette & Storey, 1981; Bahnsen et al., 1988; Grard, 1997; Geiswiller et al., 2001;
 587 Gilet et al., 2017). To account for the finite frequency resolution, we compute the ap-
 588 parent plasma frequency using three different methods. The first method consists of iden-
 589 tifying the plasma frequency as the frequency corresponding to the maximum amplitude
 590 of the spectra (light blue line in Figure 8). This method is simple but with limited per-
 591 formances, since the difference between the *apparent* and *actual* plasma frequency is con-
 592 strained by the discretization of the MI frequency sweep.

593 The second method consists of, first, interpolating the MI spectra using a polyno-
 594 mial interpolation of second order and, second, identifying the apparent plasma frequency
 595 as the frequency corresponding to the maximum amplitude of the interpolated spectra
 596 (green line in Figure 8). Using this method we mitigate the effect of the discretization
 597 in the MI frequency sweep.

598 The third method (not shown here) consists of, first, approximating the resonant
 599 peak signature of MI spectra using a gaussian function and, second, identifying the ap-
 600 parent plasma frequency as the frequency corresponding to the maximum of such gaus-
 601 sian function. Similarly to the second method, this method too is used to mitigate the
 602 effect of the discretization in the MI frequency sweep.

603 Apparent plasma frequencies derived using these methods are shown in Figure 8
 604 in function of the distance from the emitting antennas, together with the MI spectra from
 605 which they are derived. The plasma density diagnostic performance of first and second
 606 method is shown in Figure 9 (top and middle panels, respectively).

607 Using this third method, the plasma density relative errors range between 6% and
 608 50%. As they significantly exceed the uncertainty of 10%, our analysis indicates that the
 609 resonant peak of MI spectra is not well approximated by a gaussian function and there-
 610 fore this third method shall not be used for experimental applications.

611 For experimental space applications, we suggest the use of the second method (mid-
 612 dle panel of Figure 9), for which the plasma density estimation errors, ranging between
 613 0% and 12%, are minimized. The error on plasma density diagnostic due to plasma non-
 614 linearities remain below 5% (resp. 12%) for emission amplitudes corresponding to $\alpha <$
 615 0.1 (resp. $\alpha = 1$). These errors are smaller than (resp. of the order of) the instrum-
 616 ental density resolution of 10% (gray shaded area in top and middle panels of Figure 9),
 617 associated to a frequency resolution of 5%. We conclude that the plasma density diag-
 618 nostic performance of MI experiments is robust against the generation of non-linear plasma
 619 effects by strong antenna amplitude emissions.

620 4.3 Electron Temperature Diagnostic Performance for Strong Antenna 621 Emission Amplitudes

622 We here focus on evaluating the electron temperature diagnostic performance and
 623 robustness of MI experiments when using finite amplitude antenna electric emissions,
 624 likely to trigger non-linear effects in the diagnosed plasma. We do so in three steps. First,
 625 we identify the apparent plasma density ($n_{e,app.}$) from MI spectra as described in the pre-
 626 vious section. Second, we identify from the MI spectra the ratio between the (known)

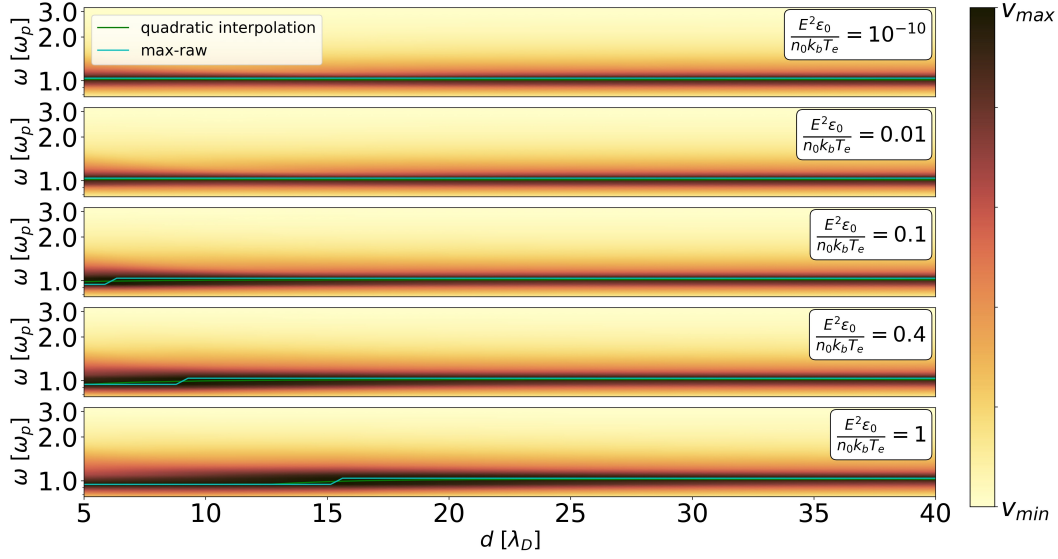


Figure 8. MI dynamic spectra in function of the emitting-receiving antennas distance d . Each spectrum, normalized for the corresponding spectrum in vacuum, is represented between its minimum and maximum amplitudes. The plasma frequency is identified as the frequency of (i) the maximum of each spectrum (light blue line), (ii) the maximum of the quadratic interpolation of each spectrum (green line).

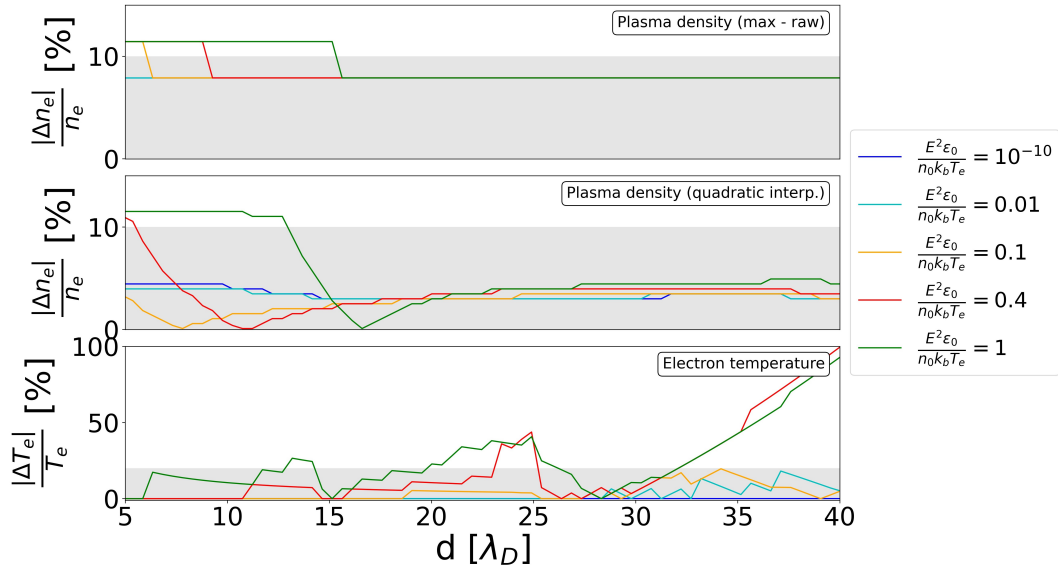


Figure 9. MI plasma density and electron temperature diagnostic performance in function of the emitting-receiving antennas distance d . The diagnostic performance is obtained for electric-to-thermal energy ratios between 10^{-10} and 1 (solid lines). Plasma density resolution of 10% and electron temperature uncertainty of 20% represented as gray shaded areas. Plasma density relative errors obtained identifying the plasma frequency as the maximum of each spectrum (top panel) or the maximum of the quadratic interpolation of each spectrum (middle panel). Electron temperature relative error identified comparing the investigated spectra to reference spectra (bottom panel).

627 emitting-receiving antennas distance and the (unknown) Debye length, hereafter called
 628 *apparent* Debye length $\lambda_{D,app.} = \sqrt{(\epsilon_0 k_B T_{e,app.}) / (e^2 n_{e,app.})}$, from which the *apparent*
 629 temperature ($T_{e,app.}$) is obtained. Third, we evaluate the electron temperature diagnos-
 630 tic performance as the relative error between this *apparent* temperature and the *actual*
 631 (T_e) electron temperature we aim to measure.

$$\frac{\|\Delta T_{e,app.}\|}{T_e} = \frac{\|T_e - T_{e,app.}\|}{T_e} = \left\| 1 - \frac{T_{e,app.}}{T_e} \right\| \quad (6)$$

632 This is done for the same emission amplitudes and emitting-receiving antennas distances
 634 as investigated in the previous section.

635 In previous space experiments, different techniques were used to derive the elec-
 636 tron temperature from MI spectra in unmagnetised Maxwellian plasma. We hereafter
 637 recall three of those.

638 The first technique is based on identifying the frequencies at which anti-resonant
 639 signatures (i.e. local minima) are spotted on MI spectra (Geiswiler et al., 2001). Anti-
 640 resonances indicate that, for the corresponding frequencies, the wavelength of the wave
 641 emitted in the plasma is a multiple of the emitting-receiving antennas' distance d at which
 642 the MI spectrum is obtained. For anti-resonances to be spotted, the emitted electric fluc-
 643 tuations reaching the receiving antennas and used to build the spectra need to be com-
 644 posed of both the cold plasma electric field term (so-called far-field term) and the prop-
 645 agating wave term (so-called close-field term). Due to propagation effects, the close-field
 646 electric fluctuations, propagating in the plasma at group velocity, reach the positions of
 647 the receiving antennas after the delay time $t_d = 2d/v_g$, where, for the anti-resonance
 648 to occur, d is expected to be a multiple of the wavelength of the emitted wave. For the
 649 emitted frequency ω , the delay time corresponds to $N_d = t_d/T$ repetitions of the os-
 650 cillation period. Considering that the reception time period is synchronized to the emis-
 651 sion, anti-resonances are expected to be spotted on the spectra if the delay time is neg-
 652 ligible w.r.t. the total reception time period, corresponding to $N \gg N_d$. For exam-
 653 ple, with a MI elementary sinusoidal signal emitted at $\omega = 1.1\omega_p$, the wavelength is $d \simeq$
 654 $25.7\lambda_D$, the group velocity corresponds to $v_g = 0.67v_{the}$ and the delay amount of rep-
 655 etitions $N_d \simeq 14$. Since in this study we focus on emission time periods correspond-
 656 ing to $N = 15$, anti-resonances are not expected to be spotted. As a consequence, this
 657 technique, designed for long emission durations, is discarded.

658 The second technique is based on the amplitude sharpness of the resonant peak of
 659 MI spectra (Chasseriaux et al., 1972; Décreau et al., 1978). This technique is also dis-
 660 carded here, since perturbations of MI spectra due to non-linear effects are enhanced at
 661 frequencies close to the plasma frequency (as found on section 3.2 and section 4.1).

662 The third technique is based on a direct comparison between the experimental spec-
 663 trum and different reference spectra (Wattiaux et al., 2020), which are theoretical spec-
 664 tra obtained assuming linear perturbations of the probed homogeneous plasma.

665 In our study, we use this third technique to identify the electron temperature as-
 666 sociated to each *synthetic* MI spectrum.

667 We use as reference spectra those obtained for emission amplitudes corresponding
 668 to electric-to-thermal energy ratio $\alpha = 10^{-10}$, corresponding to a linear plasma response,
 669 i.e. to negligible perturbations of the plasma dielectric. These reference spectra are ob-
 670 tained for emitting-receiving antennas distances d_f .

671 To each *synthetic* spectrum, we associate a *reference* spectrum, hereafter called *match-*
 672 *ing* spectrum, defined as the one that minimizes the root mean squared error $\xi = \sqrt{\sum (x_i - y_i)^2 / L}$,
 673 where L is the amount of emitted frequencies for each spectrum, x_i and y_i are the Fourier
 674 components corresponding to the i -th emitted frequency for the compared synthetic
 675 and reference spectra, respectively. To mimic typical experimental applications of this
 676 technique, the (known) actual plasma density of the reference spectra is imposed equal
 677 to the apparent plasma density of the synthetic spectrum (e.g. $n_{e,app.} = n_e$). As a con-
 678 sequence, this procedure is applied after the plasma frequency of the synthetic spectrum

679 is identified following the procedure described in the previous section. From the emitting-
 680 receiving antennas distance corresponding to the matching spectrum, we estimate an ap-
 681 parent distance associated to the synthetic spectrum as $d_{app.} = d_f$. Because of non-linear
 682 effects that might perturb the MI spectra, this apparent distance might differ from the
 683 actual distance d at which the synthetic spectrum is obtained. Both the apparent and
 684 actual distances correspond to the same *physical* distance:

$$685 \quad d_{ph} = d_{app.} \lambda_{D,app.} = d \lambda_D \quad (7)$$

686 where d_{ph} is the (non-normalized) physical distance between emitting and receiving an-
 687 tennas, fixed by design of the MI instrument, $\lambda_{D,app.}$ the apparent Debye length and λ_D
 688 the actual Debye length. From the ratio between d and $d_{app.}$ we derive the electron tem-
 689 perature relative error as:

$$690 \quad \frac{\|\Delta T_{e,app.}\|}{T_e} = \left\| 1 - \frac{n_{e,app.}}{n_e} \left(\frac{d}{d_{app.}} \right)^2 \right\| = \left\| 1 - \left(\frac{d}{d_{app.}} \right)^2 \right\| \quad (8)$$

691 In previous MI space applications, the uncertainty associated to this third technique was
 692 estimated of the order of 10% – 30% (Décréau et al., 1978). In our study, in order to
 693 mimic experimental MI applications, we consider this technique robust against strong
 694 antenna emission amplitudes if the electron temperature relative error is below the thresh-
 695 old of 20%, hereby called *reference uncertainty*.

696 In our first attempt, we find significant electron temperature relative errors for the
 697 emission amplitude corresponding to the electric-to-thermal energy ratio of 1 (not shown
 698 here). These errors are above the reference uncertainty because in the comparison pro-
 699 cess is included also the resonant signature of MI spectra, for which enhanced pertur-
 700 bations are observed for strong emission amplitudes. Therefore, to improve the robust-
 701 ness of the process and reduce the electron temperature relative errors, we now modify
 702 the third technique by discarding the contribution of the resonant peak. We do so by
 703 filtering out, before the comparison, the Fourier components of MI spectra that corre-
 704 spond to frequencies below a given threshold frequency. In the range $1.0 \omega_p$ to $2.0 \omega_p$,
 705 the best electron temperature diagnostic performances are found for the threshold fre-
 706 quency of $1.9 \omega_p$. The difference between the third technique and the improved third tech-
 707 nique is illustrated in Figure 10. Using the third technique, the electron temperature is
 708 obtained by comparing one given experimental (investigated) spectrum (green line) to
 709 several different reference spectra (blue line). Using the improved third technique, the
 710 same comparison is performed but not using the full spectra: we use only a subpart of
 711 the spectra (i.e. the gray region) and discard the resonant peak, for which strong per-
 712 turbations due to non-linear plasma interactions are expected.

713 Using this modified third technique, we find that for $\alpha = 1$ the electron temper-
 714 ature relative errors (green line in Figure 9 bottom panel) significantly exceed the ex-
 715 pected temperature uncertainty (gray shaded area) for distances above $d \geq 34 \lambda_D$. Since
 716 smaller α correspond to smaller electron temperature errors (as shown in Figure 9), a
 717 trade-off is required between (i) sufficiently strong emission amplitudes that ensure sig-
 718 nificant signal-to-noise ratios for MI measurements and (ii) small temperature relative
 719 errors. Practically, we have identified the largest MI emission amplitude (colored lines
 720 in Figure 9) for which the electron temperature relative errors remain lower than the ref-
 721 erence uncertainty (gray shaded area). In the investigated range of emitting-receiving
 722 antennas distances, we find that the maximum emission amplitude for which the elec-
 723 tron temperature identification uncertainty is *always below* the reference uncertainty cor-
 724 responds to $\alpha = 0.1$.

725 We conclude that, in 1D, the electron temperature identification process is affected
 726 by strong emission amplitudes. Small electron temperature diagnostic performance loss
 727 is ensured by perturbing the plasma with emission amplitudes corresponding to $\alpha \leq 0.1$.
 728 In section 5, we discuss, on the basis of the results of our 1D investigation, what perfor-
 729 mances we expect for 3D MI experimental applications.

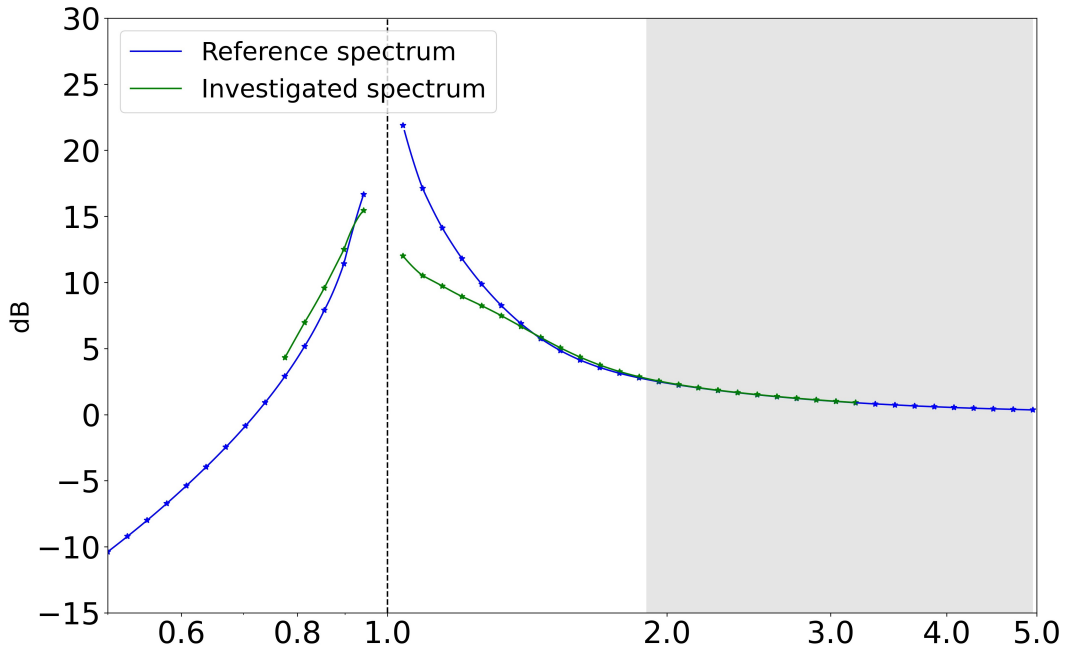


Figure 10. Illustration of the difference between the third technique and the improved third technique (gray region) for the identification of the electron temperature. Blue line represents the reference spectrum; green line represents the experimental (investigated) spectrum. The two spectra are computed for $\alpha = 10^{-10}$ and $\alpha = 1$ at distance $d = 5\lambda_D$. Using the third technique we compare the full spectra. Using the improved third technique we only compare the subpart of the spectra corresponding to the gray region.

Our results suggest that only small modifications of the signatures of the normalized MI spectra are expected due to the excitation of non-linear effects. Therefore, in the case of experimental space applications, the use of an abacus of *reference* MI spectra might facilitate the identification process of the electron temperature. Note that this abacus should be derived for the particular MI experimental application of interest. In particular, it should consider both the specific geometric configuration of the spacecraft on which the instrument is mounted and the configuration of the MI instrument itself.

4.4 Diagnostic Impact of *Consecutive* vs *Separate* Emission of Successive Frequencies

The MI emission signal is a composition of different elementary signals, each one corresponding to a different frequency. In the case of experimental MI space applications, MI spectra are built from the electric oscillations triggered in the plasma by the *consecutive* emission of all different elementary signals. In our investigation, instead, we simulate the perturbations of each elementary signal *separately*, performing different numerical simulations. In doing so, we *separate* the contributions of the different elementary signals and neglect any possible coupling between electric oscillations corresponding to different emitted frequencies. Practically, this corresponds to waiting for the plasma to regain its resting and unperturbed state between the emission of two successive elementary signals. While, for experimental space applications, this assumption is not always valid, in our investigation it is motivated by computational reasons. Indeed, the numerical investigation of the non-linear effects triggered by MI experiments requires a very large and detailed spatial domain. Such spatial domain coupled with a very fine velocity resolution mesh (mesh details given in Appendix C) results in unfeasible numerical simulations of the whole consecutive set of successive elementary signals.

Hereby, we quantify the error made when the coupling between plasma oscillations corresponding to the consecutive emission of different frequencies is neglected. To do so, we compare the MI spectra obtained from the (i) *separate* or (ii) *consecutive* emission of given elementary signals. To this purpose, we build MI spectra, following the procedure described in section 4.1, from the electric oscillations generated by the emission of elementary signals at frequencies $\omega_1 = 1.1\omega_p$, $\omega_2 = 1.32\omega_p$ and $\omega_3 = 1.584\omega_p$, for antenna emission amplitudes corresponding to electric-to-thermal energy ratios of $\alpha \simeq 10^{-10}$ and $\alpha \simeq 10^{-1}$. These frequencies are chosen because they discretize a large portion of the MI resonant peak signature, for which the perturbations due to finite antenna emission amplitudes are enhanced. For computational reasons, the perturbations are obtained for antenna emission amplitudes corresponding to an electric-to-thermal energy ratio up to $\alpha \simeq 10^{-1}$.

From the comparison between MI spectra obtained simulating (i) separately or (ii) consecutively the emission of different elementary signals, we find a maximum discrepancy of about $2dB$. While this error exceeds the typical instrumental noise level of MI experimental space applications (which is also neglected), it still is of the same order. Due to such limited perturbations, we simplify the investigation and perform our numerical simulations by avoiding the consecutive emission of the different elementary signals.

4.5 Reduced Ion-to-Electron Mass Ratio and Limited MI Emission Time Period

In this section, we briefly discuss the choice of discarding representative ion-to-electron mass ratios like the proton-to-electron mass ratio $m_i/m_e \simeq 1836$ in favor of the reduced mass ratio $m_i/m_e = 100$ for the investigation of MI diagnostic performance.

For experimental MI space applications, the amount of repetitions is typically chosen between $N = 10$ and $N = 100$ while in this analysis, for computational reasons,

779 is set to $N = 15$. While the dependency of MI diagnostic performances on the amount
780 of emitted repetitions, N , is outside the scope of this study, longer emission time peri-
781 ods indeed correspond to stronger non-linear perturbations of the plasma. In order to
782 account for the selected limited amount of repetitions and investigate the perturbations
783 of the MI diagnostic due to non-linear effects that would develop in the plasma for longer
784 emission time periods, we choose to enhance the ion dynamics by increasing the ion acous-
785 tic frequency. In particular, for our investigation, we choose a reduced ion-to-electron
786 mass ratio of $m_i/m_e = 100$ that enhances the ions' acoustic frequency by a factor \geq
787 4.

788 5 Conclusions

789 Mutual Impedance instruments are in situ, active, electric experiments that pro-
790 vide plasma diagnostics, used to identify the plasma density and electron temperature
791 in space plasmas. Such plasma parameters are derived from MI spectra which are ob-
792 tained by actively perturbing the plasma to be diagnosed with a set of emitting anten-
793 nas, while simultaneously retrieving the electric fluctuations generated in the same plasma.
794 In practical instrumental design, the choice of the antenna emission amplitude is always
795 the result of a trade-off. On the one hand, small antenna emission amplitudes ensure both
796 small perturbations to other payload instruments and a linear plasma response. On the
797 other hand, large emission amplitudes ensure signal-to-noise ratios suitable for both den-
798 sity and temperature identification. But, at the same time, they might trigger non-linear
799 electric perturbations which could affect the plasma diagnostic. In particular, diagnos-
800 tic performance loss is expected when the electric energy of the emitted signal is large
801 w.r.t. the electron thermal energy. In this study, for the first time, we relax in the mod-
802 elling of MI experiments the hypothesis of a linear plasma response and investigate nu-
803 merically the non-linear plasma perturbations on MI spectra generated by such exper-
804 iments using the 1D-1V non-linear Vlasov-Poisson model.

805 We identify, for the first time, the maximum antenna emission amplitude that can
806 be implemented to ensure robust and satisfactory diagnostic performances for both the
807 plasma density and the electron temperature. In particular, we find that for antenna emis-
808 sion amplitudes corresponding to electric-to-thermal energy ratios up to 0.1 the relative
809 errors on plasma density and electron temperature remain below 5% and 20%, respec-
810 tively.

811 In situ space plasma observations performed in the solar wind by the STEREO space-
812 craft have shown that non-linear effects are present, in the range of frequency also used
813 in MI experiments (i.e. close to the plasma frequency), for electric fluctuations of the
814 plasma corresponding to electric-to-thermal energy ratios of $\alpha = 10^{-4}$ (Henri et al., 2011).
815 For such energy ratios, our 1D numerical simulations show instead that negligible non-
816 linear perturbations of MI spectra are expected. This means that, in the short MI emis-
817 sion duration, the growth time-rate associated to the non-linear effects triggered by such
818 emission amplitude is not sufficient to develop perturbations that can significantly mod-
819 ify the spectra. Indeed, for larger antenna emission amplitudes the growth time-rate of
820 the non-linear perturbations of the plasma is enhanced and modifications of the synthetic
821 MI spectra are observed.

822 We note that our study suffers different limitations due to the numerical model we
823 used. First, the use of our Vlasov-Poisson model prevented us from investigating emis-
824 sion amplitudes that corresponded to electric-to-thermal energy ratios significantly larger
825 than 1, for which we found unstable numerical runs. Second, in our study the plasma
826 nearby the antennas is assumed as homogeneous. In experimental space applications it
827 is not the case, as plasma inhomogeneities (e.g. the antennas plasma sheath) envelope
828 the antennas and affect the propagation of plasma waves. Dedicated studies will be per-
829 formed in the near future to investigate how plasma inhomogeneities specifically affect

MI measurements. Third, in our 1D description, the emitting antennas are modeled as infinite transparent plane grids. While the classic spherical or cylindrical shapes of MI antennas used for space application cannot be simulated, this choice enabled a significant simplification of the model. To investigate the impact of the antennas' shape on the MI measurements, models such as the DSCD model (Geiswiler et al., 2001; Watteaux, G. et al., 2019) could be used. However, these models are limited to the linear regime thus preventing the analysis in the presence of plasma non-linearities.

It is important to emphasize that our results overestimate the errors expected in the case of actual experimental measurements. Indeed, in our 1D numerical investigation, the electric field amplitudes remain mostly constant with the distance (far-field and close-field electric field components discussed in section 2). Instead, in experimental 3D applications, the electric field oscillation amplitudes decrease with the distance from the emitting antennas in $1/d_{ph.}^2$, so that the electric-to-thermal energy ratio therefore decreases in $1/d_{ph.}^4$. Nevertheless our investigation represents the first step for the study of the non-linear plasma-antenna regime. For instance, let us consider a large amplitude MI emission ($\alpha = 1$) that triggers significant non-linear effects at a distance of 1 m from the emitting antennas. At a distance of 10 m, we expect significantly smaller non-linear perturbations as the electric field decreases by a factor 10^2 and α decreases by a factor 10^4 . In other words, non-linear perturbations are likely to occur only in the vicinity of the emitting antenna. Thus, the maximum amplitude identified in this work (corresponding to $\alpha = 0.1$) is to be considered a conservative, lower value that ensures negligible plasma density and electron temperature identification errors. In order to go beyond this conservative maximum amplitude and account for both a fully realistic instrumental geometry and the associated spherical radial dependence of the potential, one would need to use a multidimensional (3D-3V) Vlasov-Poisson model that would be extremely demanding computationally and out of reach of current supercomputers. This is out of the scope of this current paper but might be addressed in the future when computational resources allows it.

Part of the results found in our study are also applicable to another kind of active electric experiments dedicated to in situ space plasma diagnostics, namely the so-called relaxation sounder experiments (hereafter called RS), such as the RS experiment (J. Trotignon et al., 1986) onboard the NASA ISEE spacecraft, the RS experiment (Harvey et al., 1979) onboard the ESA GEOS spacecraft, the wave experiment (Décréau et al., 1987) onboard the Swedish VIKING spacecraft, the RS experiment of the URAP instrument (Osherovich et al., 1993) onboard the NASA/ESA Ulysses spacecraft and the WHISPER experiment (Béghin et al., 2005; J. Trotignon et al., 2003; J. G. Trotignon et al., 2010) onboard the ESA CLUSTER spacecraft. RS are based on a measurement technique similar to that of MI experiments, with the main difference that emission and reception are not simultaneous. For instance, in the case of the WHISPER instrument, emission occurs during 1ms on a long-wire antenna while reception is performed on a double-sphere antenna a few ms later, measuring waves that are able to propagate near the characteristic frequencies of the plasma. This necessitates a relatively high amplitude excitation, corresponding to an excitation voltage greater than 50V. This emission amplitude is expected to trigger electric oscillations in the plasma with energy that strongly overcomes the thermal electron energy, therefore generating non-linear plasma perturbations. Combined with the large emitting-receiving antennas distance of such experiments (WHISPER antenna are 88m in length), the high amplitude excitation allows the RS experiment probing a volume much larger w.r.t. the volume probed with MI experiments. On the one hand, non-linear effects are triggered by the large amplitude excitation. But, on the other hand, given the electric field amplitude decrease in distance as $1/d_{ph.}^2$, their influence is minimized in the overall response measured by the instrument. Moreover, considering the probed volume at play and also depending on the magnetospheric regions crossed by the CLUSTER satellite, plasma inhomogeneities and non-Maxwellian electron distributions can be the main source of uncertainty. Several studies have been conducted to

884 cross-validate simultaneous measurements from MI and RS instruments (Décréau et al.
885 (1978) on GEOS, Béghin et al. (2005) on CLUSTER).

886 Our study provides guidelines for the choice of antenna emission amplitudes of ex-
887 perimental MI applications to ensure small non-linear perturbations of the plasma den-
888 sity and electron temperature diagnostic. Note that in our study we neglect all transient
889 effects, which in the numerical simulations are damped by the chosen initialization of the
890 model (Appendix A). The possible impact of transients on MI measurements diagnos-
891 tic performance is left to future studies. Note also that these results should not concern
892 double Maxwellian electron distribution functions, for which the MI resonance might ap-
893 pear at frequencies significantly below the plasma frequency.

894 6 Open Research

895 Datasets for this research are available at Bucciantini (2022), together with a de-
896 tailed explanation on how to use them.

897 The model used to produce such dataset is described in section 2. It is based on
898 the model implemented by Mangeney et al. (2002). The 1D-1V Vlasov-Poisson version
899 of the model, which corresponds to the one we use in our investigation, is described in
900 Henri et al. (2010).

901 Acknowledgments

902 The work performed at LPC2E is supported by CNES APR. The Scientific colour map
903 "lajolla" (Crameri, 2021) is used in this study to prevent visual distortion of the data and
904 exclusion of readers with colour-vision deficiencies (Crameri et al., 2020). We acknowl-
905 edge the use of the WHAMP software Roennmark (1982) for the validation of the model.
906 We benefited from the computing resources provided by CaSciModOT. This work was
907 granted access to the HPC/AI resources of TGCC under the allocation 2021-A0100412428
908 made by GENCI. L.B. was supported by funds from Région Centre Val de Loire (France).

909 Appendix A Initialization of the Numerical Model

910 We hereby describe the initialization of the numerical simulations analyzed in this
 911 study. This initialization, based on the consistency between the Poisson and Ampère equa-
 912 tions at the beginning of each numerical simulation, removes the initial transients of the
 913 simulation by imposing, at each position, the initial current expected from the cold plasma
 914 term of the electric field (so-called far-field term).

915 The net charge at any point in the simulation box is initialized to zero and the den-
 916 sity of each species is initially uniform and equal everywhere in the simulation box.

$$917 \quad n_e(x, t = 0) = n_i(x, t = 0) = n_0 \quad (\text{A1})$$

$$918 \quad n_{net}(x, t = 0) = n_i(x, t = 0) - n_e(x, t = 0) = 0 \quad (\text{A2})$$

920 where x represents the position, t the time, n_e is the electron density, n_i is the ion den-
 921 sity, n_0 is the unperturbed plasma density and n_{net} is the total charge density. The os-
 922 cillating charges σ at the (infinite plane) emitting antennas are initialized to zero:

$$923 \quad \sigma(t = 0) = 0. \quad (\text{A3})$$

924 During the simulations, the oscillating charges at the antennas are imposed equal to $\bar{\sigma} \sin(\omega t)$,
 925 with $\bar{\sigma}$ its amplitude and ω the emission frequency. The electric field, computed from
 926 the initial net-charge, is zero everywhere in the simulation box:

$$927 \quad E(x, t = 0) = 0 \quad (\text{A4})$$

928 where E is the electric field. To ensure the consistency between the Poisson and Am-
 929 père equations at the beginning of each simulation, we initialize the current consider-
 930 ing the current injected in the plasma at the emitting antenna and considering the time
 931 derivative of the initial electric field (Podesta, 2005) at each position in the simulated
 932 box.

933 The external current density injected from the emitting antenna in the plasma, at
 934 the beginning of the simulation, reads:

$$935 \quad j_{ext}(t = 0) = \bar{\sigma} \omega \quad (\text{A5})$$

936 where $\bar{\sigma}$ is the amplitude of the homogeneous charge per unit surface on the infinite charged
 937 plane. At each position, the expected current density, in the electrostatic 1D case, reads:

$$938 \quad j_{tot}(t = 0) = -\epsilon_0 \frac{\partial E}{\partial t} \quad (\text{A6})$$

939 For emission frequencies close to the plasma frequency, the electric field reads (Podesta,
 940 2005):

$$941 \quad E = \frac{\bar{\sigma} \sin(t\omega)}{2\epsilon_0(1 - \frac{\omega_p^2}{\omega^2})} \text{sgn}(x) \quad (\text{A7})$$

942 where ω_p is the plasma frequency. The difference between the expected current density
 943 at each position and the current density sent in the plasma by the external antenna gives
 944 the initial current density we need to impose at each position in the simulation box. This
 945 current density is imposed via an offset on the velocity distribution functions with which
 946 we initialize the electrons, converting the initial Maxwellian distribution to a drifting Maxwellian.
 947 This velocity offset reads:

$$948 \quad \frac{v_{offset}}{v_{the}} = \frac{\hat{\sigma}}{2} \frac{\hat{\omega}}{\frac{\omega^2}{\omega_p^2} - 1} \quad (\text{A8})$$

949 where v_{offset} is the velocity offset of the Maxwellian distributions of the electrons at ini-
 950 tialization, v_{the} is the electron thermal velocity and $\hat{\sigma} = \sigma/\bar{\sigma}$ is the amplitude of the

951 non-dimensional charge per unit surface imposed at the emitting antennas, with $\bar{\sigma}$ the
952 planar charge distribution used to normalize the model.

953 This initialization minimizes the transients generated in the plasma when switching-
954 on the emission at the electric antennas. This initialization is used in our study both for
955 model A and model B.

956 Appendix B Validation of the Model

957 In this appendix, we describe the validation of the two models (model A and model B)
958 used in this study.

959 First, the numerical model is validated by comparing the simulated electric oscil-
960 lations in the numerical box, at given distance from the emitting antenna and at given
961 time after the beginning of the emission, against the electric oscillations expected an-
962 alytically considering temporal and spatial Landau Damping of the emitted waves. These
963 expected electric fluctuations are derived by solving the Vlasov-Poisson coupled equa-
964 tions as described, e.g., in Krall and Thrivepiece (1973), limiting the analysis to real fre-
965 quencies and complex wavenumbers. A similar computation of the analytic expressions
966 for this 1D-1V case study is described in Podesta (2005). The validation of model A (resp.
967 B) is illustrated in Panel a (resp. b) of Figure B1 as the comparison between the expected
968 electric fluctuations (black line) and the simulated electric field oscillations (red line),
969 computed for emission frequency $\omega = 1.1\omega_p$ at time $t = 100\omega_p^{-1}$ and in function of the
970 emitting-receiving antennas distance. The emitted wave-packet propagates from the emit-
971 ting antennas at group velocity and, along the distance it covers, the expected and sim-
972 ulated electric fluctuations agree. Note that limited differences are expected, since the
973 analytic approximation is derived considering only the dominant pole and neglecting higher-
974 order solutions (Podesta, 2005). The frequency-wavenumber couples used to obtain the
975 analytic electric oscillations are computed using the linear Vlasov-Maxwell solver WHAMP
976 (Roennmark, 1982), in the limit of an unmagnetized plasma. Second, we validate the MI
977 spectra obtained numerically against spectra derived using the DSCD model (Béghin &
978 Kolesnikova, 1998; Geiswiler et al., 2001; Wattiaux, G. et al., 2019; Wattiaux et al.,
979 2020) which is the reference numerical tool for the modelling of MI instrumental response
980 in the case of electrostatic linear perturbations of the plasma. This model is typically
981 used to validate MI experimental measurements because, at the state of the art, it is the
982 only MI model capable of taking into account the presence of the satellite platform when
983 deriving MI spectra. In contrast to our 1D model, the DSCD model supposes very long
984 emission periods (e.g. MI emission starts at time $t = -\infty$) and neglects the transient
985 (delay) time required by the wave-packet generated at the emitting antennas to cover
986 the receiving-emitting antennas distance.

987 The comparison between spectra is performed for different emitting-receiving an-
988 tennas distances and for antenna emission amplitudes corresponding to an electric-to-
989 thermal energy ratio of 10^{-10} . The comparison is illustrated in Figure B2 for distances
990 $d = 0.5\lambda_D$, $d = 5\lambda_D$, $d = 20\lambda_D$, $d = 40\lambda_D$. On the one hand, for d smaller than $5\lambda_D$,
991 the spectra disagree because of differences in the modelling of the emitting antennas be-
992 tween the two models. On the other hand, for d larger than $5\lambda_D$, the spectra agree. There-
993 fore, to assess the diagnostic performance of MI experiments to finite emission ampli-
994 tudes, we focus on emitting-receiving antennas distances larger than $5\lambda_D$ and neglect smaller
995 distances.

996 Appendix C Model Parameters

997 In Table C1, for completeness and repeatability purposes, we show the parameters
998 used for each numerical simulation.

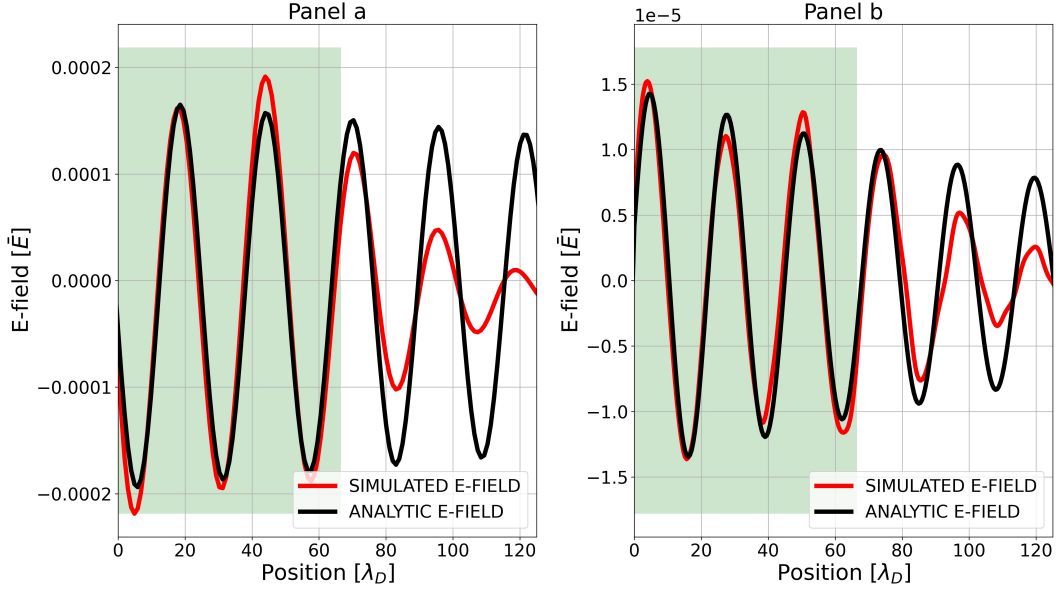


Figure B1. Validation of model A (panel A) and model B (panel b). Comparison between the electric fluctuations obtained numerically (red solid line) and those computed analytically (black solid line), in function of the emitting-receiving antennas distance, for the emission frequency $\omega = 1.1\omega_p$ and at time $t = 100\omega_p^{-1}$. At such time the emitted wave packet, propagating at group velocity $v_g = 0.67v_{the}$, has covered the distance $d = 67\lambda_D$ (green shaded area).

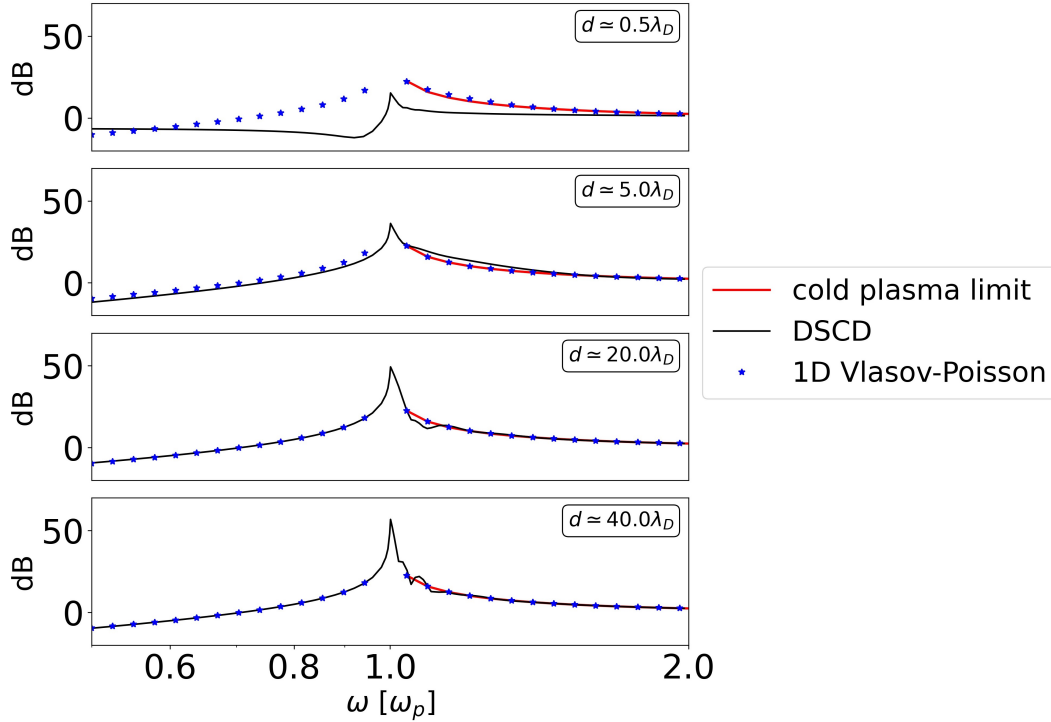


Figure B2. Comparison between spectra derived using our 1D Vlasov-Poisson model (blue points) and the DSCD model (black solid line). The red line represents the expected cold plasma response, valid for $\frac{\omega}{\omega_p} \gg 1$.

999 In Table C1 and Table C2 for completeness and repeatability purposes we show the
 1000 parameters used for each numerical simulation. Table C1 (resp. Table C2) refers to the
 1001 simulations supporting the discussion of section 3 (resp. section 4). LF (resp. SL) means
 1002 Low Fixed (resp. Sweep Low) and indicates simulations used to investigate the plasma
 1003 perturbations due to *single* fixed frequency (resp. sweep) emission(s) in the case of low
 1004 amplitudes, associated to a linear plasma response. NI (resp. SI) means Non-linear Ions
 1005 (resp. Sweep Ions) and simulate instead fixed frequency (resp. sweep) emissions in the
 1006 case of moving ions with large emission amplitudes, associated to significant perturba-
 1007 tions of the plasma. NF means Non-linear Fixed and indicates simulations supporting
 1008 the discussion of section 3.1, where we investigate plasma perturbations due to strong
 1009 amplitude signals in the case of a fixed background of positive charges. MI sweep mea-
 1010 surements are built using a number of different numerical runs with same numerical boxes
 1011 but different emitted frequency. If one line is used to indicate in Table C2 each emitted
 1012 frequency, the result would be a very long table with very diluted information. For sim-
 1013 plicity purposes and to help the reader focus on the significant information of the table,
 1014 we give instead the frequency resolution of the sweep measurement (last column of Ta-
 1015 ble C2) which one can use to extrapolate the information regarding all emitted frequen-
 1016 cies. Therefore, for each simulated MI sweep we only give two lines. One line correspond-
 1017 ing to the first emitted frequency of the sweep and one corresponding to the last frequency
 1018 of the sweep. For instance, SL_01 is the numerical simulation used to investigate the
 1019 first frequency, $\omega_{SL,01} = 0.5\omega_p$, of one sweep measurement. SL_48 is the simulation in-
 1020 vestigating the last frequency, $\omega_{SL48} = 4.95\omega_p$, of the same measurement. The rest of
 1021 the simulated frequencies of the sweep are obtained as $\omega_{n+1} = 1.05\omega_n$. We note that
 1022 the LF simulations of Table C1 have not been used in the discussion of section 3, but
 1023 rather served us as reference during the analysis.

1024 References

- 1025 Bahnsen, A., Jespersen, M., Ungstrup, E., Pottelette, R., Malingre, M., Decreau, P.,
 1026 ... Pedersen, B. (1988). First VIKING results: high frequency waves. *Physica*
 1027 *Scripta*, *37*(3), 469-474. doi: <https://doi.org/10.1088/0031-8949/37/3/032>
- 1028 Béghin, C. (1995). Series expansion of electrostatic potential radiated by a point
 1029 source in isotropic maxwellian plasma. *Radio Science*, *30*, 307-322. doi:
 1030 <https://doi.org/10.1029/94RS03167>
- 1031 Béghin, C., Décreau, P. M. E., Pickett, J., Sundkvist, D., & Lefebvre, B. (2005).
 1032 Modeling of cluster's electric antennas in space: Application to plasma diag-
 1033 nostics. *Radio Science*, *40*(6). doi: <https://doi.org/10.1029/2005RS003264>
- 1034 Béghin, C., & Debrie, R. (1972). Characteristics of the electric field far from
 1035 and close to a radiating antenna around the lower hybrid resonance in
 1036 the ionospheric plasma. *Journal of Plasma Physics*, *8*(3), 287-310. doi:
 1037 <https://doi.org/10.1017/S0022377800007157>
- 1038 Béghin, C., Karczewski, J. F., Poirier, B., Debrie, R., & Masevich, N. (1982). The
 1039 ARCAD-3 ISOPROBE experiment for high time resolution thermal plasma
 1040 measurements. *Annales de Geophysique*, *38*(5), 615-629.
- 1041 Béghin, C., & Kolesnikova, E. (1998). Surface-charge distribution approach for mod-
 1042 eling of quasi-static electric antennas in isotropic thermal plasma. *Radio Sci-*
 1043 *ence*, *33*(3), 503-516. doi: <https://doi.org/10.1029/97RS03588>
- 1044 Brunetti, M., Califano, F., & Pegoraro, F. (2000). Asymptotic evolution of nonlinear
 1045 Landau damping. *Phys. Rev. E*, *62*, 4109-4114. doi: [https://doi.org/10.1103/](https://doi.org/10.1103/PhysRevE.62.4109)
 1046 [PhysRevE.62.4109](https://doi.org/10.1103/PhysRevE.62.4109)
- 1047 Bucciardini, L. (2022). *1D-1V Vlasov-Poisson Simulations of Mutual Impedance Ex-*
 1048 *periments for Strong Antenna Emission Amplitudes*. Zenodo. doi: [https://doi](https://doi.org/10.5281/zenodo.7149358)
 1049 [.org/10.5281/zenodo.7149358](https://doi.org/10.5281/zenodo.7149358)
- 1050 Buckley, R. (1968). Radio frequency properties of a plane grid capacitor immersed
 1051 in a hot collision-free plasma. *J. Plasma Physics*, *2*, 339-351. doi: [https://doi](https://doi.org/10.1017/S0022377800007157)

Table C1. List of numerical simulation settings parameters for investigating non-linear perturbations of the plasma: total length of the simulation box (X_{max}), velocity range for the electron distribution function (V_e), velocity range for the ion distribution function (V_i), amount of spatial mesh points (n_x), amount of velocity mesh points for electrons (n_{ve}), amount of velocity mesh points for ions (n_{vi}), advancement time resolution of the simulation (dt), emission frequency (ω), oscillating charges at the antenna (σ), ion-to-electron mass ratio (m_i/m_e), ion-to-electron temperature ratio (T_i/T_e), electric-to-thermal energy ratio ($E^2/(k_B T_e)$). M represents the antennas configuration (model) used for these simulations.

Name	M	X_{max} [λ_D]	V_{maxe} [v_{the}]	v_i [v_{thi}]	n_x	n_{ve}	n_{vi}	dt [ω_p^{-1}]	ω [ω_p]	σ [$\bar{\sigma}$]	$\frac{m_i}{m_e}$	$\frac{T_i}{T_e}$	$\frac{E^2}{k_B T_e}$
LF_01	A	1000	(-25,25)	(-25,25)	2048	601	601	1e-3	0.5	1e-5	inf	0.1	1e-10
LF_02	A	1000	(-25,25)	(-25,25)	2048	601	601	1e-3	1.1	1e-5	inf	0.1	1e-8
LF_03	A	1000	(-25,25)	(-25,25)	2048	601	601	1e-3	2.0	1e-5	inf	0.1	1e-10
NF_01	A	1000	(-25,25)	(-25,25)	2048	601	601	1e-3	0.5	0.1	inf	0.1	0.01
NF_02	A	1000	(-25,25)	(-25,25)	2048	601	601	1e-3	1.1	0.1	inf	0.1	0.33
NF_03	A	1000	(-25,25)	(-25,25)	2048	601	601	1e-3	2.0	0.1	inf	0.1	0.01
NI_01	A	1000	(-25,25)	(-25,25)	2048	601	601	1e-3	0.5	0.1	100	0.1	0.01
NI_02	A	1000	(-25,25)	(-25,25)	2048	601	601	1e-3	1.1	0.1	100	0.1	0.33
NI_03	A	1000	(-25,25)	(-25,25)	2048	601	601	1e-3	2.0	0.1	100	0.1	0.01

Table C2. List of numerical simulation settings parameters for building MI spectra: total length of the simulation box (X_{max}), velocity range for the electron distribution function (V_e), velocity range for the ion distribution function (V_i), amount of spatial mesh points (n_x), amount of velocity mesh points for electrons (n_e), amount of velocity mesh points for ions (n_i), advancement time resolution of the simulation (dt), emission frequency (ω), oscillating charges at the antenna (σ), ion-to-electron mass ratio (m_i/m_e), ion-to-electron temperature ratio (T_i/T_e), frequency sweep resolution (ω_{n+1}/ω_n). M represents the antennas configuration (model) used for these simulations.

Name	M	X_{max} [λ_D]	V_{maxe} [v_{the}]	v_i [v_{thi}]	n_x	n_{te}	n_{ti}	dt [ω_p^{-1}]	ω [ω_p]	σ [$\bar{\sigma}$]	$\frac{m_i}{m_e}$	$\frac{T_i}{T_e}$	$\frac{\omega_{n+1}}{\omega_n}$
SL_01	B	4000	(-25,25)	(-25,25)	8192	601	601	1e-3	0.5	1e-5	100	0.1	1.05
SL_48	B	4000	(-25,25)	(-25,25)	8192	601	601	1e-3	4.95	1e-5	100	0.1	1.05
SI1_01	B	4000	(-25,25)	(-25,25)	8192	601	601	1e-3	0.77	0.1	100	0.1	1.05
SI1_14	B	4000	(-25,25)	(-25,25)	8192	601	601	1e-3	1.53	0.1	100	0.1	1.05
SI2_01	B	4000	(-25,25)	(-25,25)	8192	601	601	1e-3	0.77	0.31	100	0.1	1.05
SI2_14	B	4000	(-25,25)	(-25,25)	8192	601	601	1e-3	1.53	0.31	100	0.1	1.05
SI3_01	B	4000	(-25,25)	(-25,25)	8192	601	601	1e-3	0.77	0.6	100	0.1	1.05
SI3_14	B	4000	(-25,25)	(-25,25)	8192	601	601	1e-3	1.53	0.6	100	0.1	1.05
SI4_01	B	4000	(-40,40)	(-25,25)	8192	1001	601	5e-4	0.77	1.0	100	0.1	1.05
SI4_14	B	4000	(-40,40)	(-25,25)	8192	1001	601	5e-4	1.53	1.0	100	0.1	1.05

- 1052 .org/10.1017/S0022377800003871
- 1053 Califano, F., Galeotti, L., & Briand, C. (2007). Electrostatic coherent structures:
1054 The role of the ions dynamics. *Physics of Plasmas*, *14*(5), 052306. doi:
1055 https://doi.org/10.1063/1.2724807
- 1056 Califano, F., & Lontano, M. (1999). Vlasov-poisson simulations of strong wave-
1057 plasma interaction in conditions of relevance for radio frequency plasma
1058 heating. *Phys. Rev. Lett.*, *83*, 96-99. doi: https://doi.org/10.1103/
1059 PhysRevLett.83.96
- 1060 Chassériaux, J., Debrie, R., & Renard, C. (1972). Electron density and tempera-
1061 ture measurements in the lower ionosphere as deduced from the warm plasma
1062 theory of the h.f. quadrupole probe. *J. Plasma Physics*, *8*, 231-253. doi:
1063 https://doi.org/10.1017/S0022377800007108
- 1064 Chassériaux, J. M. (1972). Potential set up by a point charge oscillating in mag-
1065 nitude in an inhomogeneous plasma. *Plasma Physics*, *14*(8), 763-781. doi:
1066 https://doi.org/10.1088/0032-1028/14/8/002
- 1067 Chassériaux, J. M. (1974). Excitation of the plasma and upper hybrid resonances
1068 in a warm magnetoplasma by an alternating electric dipole. *Journal of Plasma
1069 Physics*, *11*(2), 225-252. doi: https://doi.org/10.1017/S0022377800024624
- 1070 Crameri, F. (2021). *Scientific colour maps*. Zenodo. doi: https://doi.org/10.5281/
1071 zenodo.5501399
- 1072 Crameri, F., Shephard, G. E., & Heron, P. J. (2020). The misuse of colour in science
1073 communication. *Nature Communications*, *11*. doi: https://doi.org/10.1038/
1074 s41467-020-19160-7
- 1075 Décréau, P. M. E., Beghin, C., & Parrot, M. (1978). Electron Density and Temper-
1076 ature, as Measured by the Mutual Impedance Experiment on Board GEOS-1
1077 (Article published in the special issues: Advances in Magnetospheric Physics
1078 with GEOS- 1 and ISEE - 1 and 2.). *Space Science Reviews*, *22*(5), 581-595.
1079 doi: https://doi.org/10.1007/BF00223942
- 1080 Décréau, P. M. E., Hamelin, M., Massif, R., de Feraudy, H., & Pawela, E. (1987).
1081 Plasma probing by active wave experiments on the viking satellite. *Annales
1082 Geophysicae*, *5*, 181-185.
- 1083 Dysthe, K. B., & Franklin, R. (1970). Non-linear interactions of coherent electro-
1084 static plasma waves. *Plasma Physics*, *12*(9), 705-721. doi: https://doi.org/10
1085 .1088/0032-1028/12/9/005
- 1086 Eriksson, A. I., Engelhardt, I. A. D., André, M., Boström, R., Edberg, N. J. T., Jo-
1087 hansson, F. L., ... Norberg, C. (2017). Cold and warm electrons at comet
1088 67p/churyumov-gerasimenko. *A&A*, *605*, A15. doi: https://doi.org/10.1051/
1089 0004-6361/201630159
- 1090 Geiswiler, J., Béghin, C., Kolesnikova, E., Lagoutte, D., Michau, J. L., & Trotignon,
1091 J. G. (2001). Rosetta spacecraft influence on the mutual impedance probe fre-
1092 quency response in the long debye length mode. *Planetary and Space Science*,
1093 *49*(6), 633-644. doi: https://doi.org/10.1016/S0032-0633(00)00173-2
- 1094 Gilet, N., Henri, P., Wattieaux, G., Cilibrasi, M., & Béghin, C. (2017). Electrostatic
1095 potential radiated by a pulsating charge in a two-electron temperature plasma.
1096 *Radio Science*, *52*, 1432-1448. doi: https://doi.org/10.1002/2017RS006294
- 1097 Grard, R. (1969). Coupling between two electric aerials in a warm plasma. *Alta Fre-
1098 quency*, *38*, 97-101.
- 1099 Grard, R. (1997). Influence of suprathermal electrons upon the transfer impedance
1100 of a quadrupolar probe in a plasma. *Radio Science*, *32*(3), 1091-1100. doi:
1101 https://doi.org/10.1029/97RS00254
- 1102 Harvey, C. C., Etcheto, J., & Mangeney, A. (1979). Early results from the isee
1103 electron density experiment. In K. Knott, A. Durney, & K. Ogilvie (Eds.), *Ad-
1104 vances in magnetospheric physics with geos-1 and isee* (p. 533-552). Dordrecht:
1105 Springer Netherlands. doi: https://doi.org/10.1007/978-94-009-9527-7_34
- 1106 Henri, P., Califano, F., Briand, C., & Mangeney, A. (2010). Vlasov-poisson sim-

- 1107 ulations of electrostatic parametric instability for localized langmuir wave
 1108 packets in the solar wind. *Journal of Geophysical Research*, *115*, A06106. doi:
 1109 https://doi.org/10.1029/2009JA014969
- 1110 Henri, P., Califano, F., Briand, C., & Mangeney, A. (2011). Low-energy langmuir
 1111 cavitons: Asymptotic limit of weak turbulence. *EPL (Europhysics Letters)*,
 1112 *96*(5), 55004. doi: https://doi.org/10.1209/0295-5075/96/55004
- 1113 Henri, P., Vallières, X., Hajra, R., Goetz, C., Richter, I., Glassmeier, K.-H., ... Wat-
 1114 tieaux, G. (2017). Diamagnetic region(s): structure of the unmagnetized
 1115 plasma around comet 67p/cg. *Monthly Notices of the Royal Astronomical*
 1116 *Society*, *469*, S372-S379. doi: https://doi.org/10.1093/mnras/stx1540
- 1117 Kasaba, Y., Kojima, H., Moncuquet, M., Wahlund, J., Yagitani, S., Sahraoui, F.,
 1118 ... Usui, H. (2020). Plasma Wave Investigation (PWI) Aboard BepiColombo
 1119 Mio on the Trip to the First Measurement of Electric Fields, Electromagnetic
 1120 Waves, and Radio Waves Around Mercury. *Space Science Reviews*, *216*(65).
 1121 doi: https://doi.org/10.1007/s11214-020-00692-9
- 1122 Krall, N., & Trivelpiece, A. (1973). *Principles of plasma physics*. McGraw-Hill.
- 1123 Mangeney, A., Califano, F., Cavazzoni, C., & Travniecek, P. (2002). A Numerical
 1124 Scheme for the Integration of the Vlasov-Maxwell System of Equations.
 1125 *Journal of Computational Physics*, *179*. doi: https://doi.org/10.1006/
 1126 jcp.2002.7071
- 1127 Odelstad, E., Eriksson, A. I., André, M., Graham, D. B., Karlsson, T., Vaivads,
 1128 A., ... Stenberg-Wieser, G. (2020). Plasma density and magnetic field
 1129 fluctuations in the ion gyro-frequency range near the diamagnetic cavi-
 1130 ty of comet 67P. *Journal of Geophysical Research Space Physics*. doi:
 1131 https://doi.org/10.1029/2020JA028192
- 1132 O'Neil, T. (1965). Collisionless damping of nonlinear plasma oscillations. *The*
 1133 *Physics of Fluids*, *8*(12), 2255-2262. doi: https://doi.org/10.1063/1.1761193
- 1134 Osherovich, V. A., Benson, R. F., Fainberg, J., Stone, R. G., & MacDowall,
 1135 R. J. (1993). Souder stimulated d_n resonances in jupiter's io plasma
 1136 torus. *Journal of Geophysical Research*, *98*(E10), 18751-18756. doi:
 1137 https://doi.org/10.1029/93JE01481
- 1138 Podesta, J. J. (2005). Spatial landau damping in plasmas with three-dimensional k
 1139 distributions. *Physics of plasmas*, *12*. doi: https://doi.org/10.1063/1.188547
- 1140 Pottelette, R., Rooy, B., & Fiala, V. (1975). Theory of the mutual impedance of two
 1141 small dipoles in a warm isotropic plasma. *Journal of Plasma Physics*, *14*(2),
 1142 209-243. doi: https://doi.org/10.1017/S0022377800009533
- 1143 Pottelette, R., & Storey, L. R. O. (1981). Active and passive methods for the
 1144 study of non-equilibrium plasmas using electrostatic waves. *Journal of Plasma*
 1145 *Physics*, *25*(2), 323-350. doi: https://doi.org/10.1017/S0022377800023151
- 1146 Roennmark, K. (1982). *Waves in homogeneous, anisotropic multicomponent plasmas*
 1147 (*whamp*).
- 1148 Rooy, B., Feix, M. R., & Storey, L. R. O. (1972). Theory of a quadripolar probe for
 1149 a hot isotropic plasma. *Plasma Physics*, *14*(3), 275-300. doi: https://doi.org/
 1150 10.1088/0032-1028/14/3/005
- 1151 Snodgrass, C., & Jones, G. H. (2019). The european space agency's comet intercep-
 1152 tor lies in wait. *Nature Communications*, *10*(5418). doi: https://doi.org/10
 1153 .1038/s41467-019-13470-1
- 1154 Storey, L., Aubry, L., & Meyer, P. (1969). Mutual impedance techniques for
 1155 space plasma measurements. *In Measurement techniques in space plasmas -*
 1156 *Fields, Geophysical Monograph Series*, *103*, 155. doi: https://doi.org/10.1029/
 1157 GM103p0155
- 1158 Tkachenko, A., Krasnoselskikh, V., & Voshchepynets, A. (2021). Harmonic ra-
 1159 dio emission in randomly inhomogeneous plasma. *The Astrophysical Journal*,
 1160 *908*(2), 126. doi: https://doi.org/10.3847/1538-4357/abd2bd
- 1161 Trotignon, J., Béghin, C., Lagoutte, D., Michau, J., Matsumoto, H., Kojima,

- 1162 H., ... Pottellette, R. (2006). Active measurement of the thermal elec-
 1163 tron density and temperature on the mercury magnetospheric orbiter of the
 1164 bepicolombo mission. *Advances in Space Research*, 38(4), 686-692. doi:
 1165 <https://doi.org/10.1016/j.asr.2006.03.031>
- 1166 Trotignon, J., Etcheto, J., & Thouvenin, J. (1986). Automatic determination of the
 1167 electron density measured by the relaxation sounder on board ISEE 1. *Journal*
 1168 *of Geophysical Research Space Physics*, 91(A4), 4302. doi: [https://doi.org/10](https://doi.org/10.1029/JA091iA04p04302)
 1169 [.1029/JA091iA04p04302](https://doi.org/10.1029/JA091iA04p04302)
- 1170 Trotignon, J., et al. (2007). RPC-MIP: The Mutual Impedance Probe of the Rosetta
 1171 Plasma Consortium. *Space Science Reviews*, 128, 713-728.
- 1172 Trotignon, J., Rauch, J., Décréu, P., Canu, P., & Lemaire, J. (2003). Active and
 1173 passive plasma wave investigations in the earth's environment: The clus-
 1174 ter/whisper experiment. *Advances in Space Research*, 31(5), 1449-1454. doi:
 1175 [https://doi.org/10.1016/S0273-1177\(02\)00959-6](https://doi.org/10.1016/S0273-1177(02)00959-6)
- 1176 Trotignon, J. G., Décréau, P. M. E., Rauch, J. L., Vallières, X., Rochel, A., Kouglé-
 1177 nou, S., ... Masson, A. (2010). The whisper relaxation sounder and the cluster
 1178 active archive..
- 1179 Wattieaux, G., Henri, P., Gilet, N., Vallières, X., & Deca, J. (2020). Plasma char-
 1180 acterization at comet 67p between 2 and 4 au from the sun with the rpc-mip
 1181 instrument. *A&A*, 638, A124. doi: [https://doi.org/10.1051/0004-6361/](https://doi.org/10.1051/0004-6361/202037571)
 1182 [202037571](https://doi.org/10.1051/0004-6361/202037571)
- 1183 Wattieaux, G., Gilet, N., Henri, P., Vallières, X., & Bucciantini, L. (2019). Rpc-
 1184 mip observations at comet 67p/churyumov-gerasimenko explained by a model
 1185 including a sheath and two populations of electrons. *A&A*, 630, A41. doi:
 1186 <https://doi.org/10.1051/0004-6361/201834872>
- 1187 Youssef, E. (1996). Ecsc - european cooperation for space standardization. In
 1188 *Space programs and technologies conference*. doi: [https://doi.org/10.2514/](https://doi.org/10.2514/6.1996-4305)
 1189 [6.1996-4305](https://doi.org/10.2514/6.1996-4305)
- 1190 Zakharov, V. E., & Karpman, V. I. (1963). On the nonlinear theory of the damping
 1191 of plasma waves. *Soviet Journal of Experimental and Theoretical Physics*, 16,
 1192 351.